CHALMERS
UNIVERSITY OF TECHNOLOGY

Investigation of loss, torque ripple and tooth forces of an ASM with sinusoidal and PWM feeding

Master's thesis in Sustainable Electric Power Engineering and Electromobility

BINAYA ADHIKARI
OSKAR BLOM

DEPARTMENT OF ELETRICAL ENGINEERING

CHALMERS UNIVERSITY OF TECHNOLOGY
Gothenburg, Sweden 2023
www.chalmers.se

MASTER'S THESIS 2023

Investigation of loss, torque ripple and tooth forces of an ASM with sinusoidal and PWM feeding

BINAYA ADHIKARI
OSKAR BLOM

CHALMERS
UNIVERSITY OF TECHNOLOGY

Department of Electrical Engineering
Division of Electric Power Engineering
CHALMERS UNIVERSITY OF TECHNOLOGY
Gothenburg, Sweden 2023

Investigation of loss, torque ripple and tooth forces of an ASM with sinusoidal and PWM feeding

BINAYA ADHIKARI
OSKAR BLOM

Supervisor: Torbjörn Thiringer, Department of Electrical Engineering
Supervisor: Joachim Härsjö, Volvo Cars Corporation
Examiner: Torbjörn Thiringer, Department of Electrical Engineering

Master's Thesis 2023
Department of Electrical Engineering
Division of Electrical Power Engineering
Chalmers University of Technology
SE-412 96 Gothenburg
Telephone +46 31 772 1000

Typeset in LaTeX
Printed by Chalmers Reproservice
Gothenburg, Sweden 2023

Investigation of loss, torque ripple and tooth forces of an ASM with sinusoidal and PWM feeding

BINAYA ADHIKARI
OSKAR BLOM
Department of Electrical Engineering
Chalmers University of Technology

Abstract

This thesis compares the performance of induction motor when supplied with purely sinusoidal input and PWM on with focus on the motor characteristics such as tooth forces, torque ripple and losses. A minimum loss control algorithm is employed based on the inverse gamma model of IM where core losses are modelled as the losses in the equivalent core resistance.The IM was modelled in Finite Element Method (FEM) software called ANSYS Maxwell.

Keywords: Electric Vehicles,PMSM, IM, FEM, Tooth Force, Torque Ripples, Loss, Minimum Loss Control, PWM .

Acknowledgements

We would like to express our utmost gratitude and appreciation to our exceptional supervisor and examiner, Torbjörn Thiringer. His unwavering support, invaluable guidance, and insightful suggestions have been instrumental in shaping the success of this thesis.

We are deeply grateful to Joachim Härsjö, our supervisor at Volvo Cars Corporation, for his unwavering support and motivation. His invaluable assistance and profound insights have played a pivotal role in the successful completion of this thesis.

Finally, I, Binaya, would like to express my sincere gratitude to the Swedish Institute (SI) for funding my master's program at Chalmers University of Technology.

Oskar Blom and Binaya Adhikari, Gothenburg, June 2023

List of Acronyms

Below is the list of acronyms that have been used throughout this thesis listed in alphabetical order:

IM	Induction Motor
PMSM	Permanent Magnet Synchronous Motor
MPTA	Maximum Torque Per Ampere
MLC	Minimum Loss Control
EMF	Electromotive Force
FEM	Finite Element Method
KVL	Kirchhoff Voltage Law
FFT	Fast Fourier transform
EV	Electric Vehicle

Nomenclature

Below is the nomenclature of indices, sets, parameters, and variables that have been used throughout this thesis.

η	Efficiency
μ_0	Permeability of Vacuum [H/m]
Ω_r	Mechanical Rotor Frequency [rad/s]
ω_r	Electrical Rotor Frequency [rad/s]
Ω_s	Stator Synchronous Frequency divided by number of pole pairs[rad/s]
ω_s	Synchronous Frequency [rad/s]
ρ_{al}	Aluminium Resistivity [Ωm]
ρ_{cu}	Copper Resistivity [Ωm]
Ψ_r	Fluxlinkage of Rotor [Ωm]
$\underline{I}_c$	Core Loss Current Phasor [A]
$\underline{I}_m$	Magnetizing Current Phasor [A]
$\underline{I}_r$	Rotor Current Phasor [A]
$\underline{I}_s$	Stator Current Phasor [A]
$\underline{I}_m$	Magnetizing Current Phasor [A]
$\underline{i}_c$	Core Loss Current Space Vector [A]
$\underline{i}_m$	Magnetizing Current Vector [A]
$\underline{i}_r$	Rotor Current Space Vector [A]
$\underline{i}_s$	Stator Current Vector [A]
$\underline{U}_m$	Magnetizing Voltage Phasor [A]
$\underline{U}_s$	Stator Volatge Phasor [A]
$\underline{u}_s$	Stator Volatge Space Vector [A]
A_{cond}	Conductor Cross Section Area [m^2]
$A_{r,slot}$	Rotor Bar Cross Section Area [m^2]

A_{scr}	Short Circuit Ring Cross Section Area [m^2]
C_s	Number of Parallel Branches
f	Supply Frequency [Hz]
h_{ew}	Stator End Winding Height [m]
h_{gap}	Airgap Length [m]
h_{r0}	Rotor Slot Opening Height [m]
h_{r1}	Rotor Slot Closing Height [m]
h_{r2}	Rotor Slot Body Height [m]
h_{s0}	Stator Slot Opening Height [m]
h_{s1}	Stator Slot Closing Height [m]
h_{s2}	Rotor Slot Body Height [m]
I_m	Magnetizing Current Magnitude [A]
I_r	Rotor Current Magnitude [A]
I_s	Stator Current Magnitude [A]
$I_{s,max}$	Maximum Stator Current [A]
i_{sd}	Stator Current in d-direction [A]
i_{sq}	Stator Current in q-direction [A]
k_1	Winding Factor for the Fundamental Frequency
L_m	Magnetising Inductance in Gamma Model [H]
L_σ	Leakage Inductance in Gamma Model [H]
L_s	Stator Leakage Inductance [H]
L_{bar}	Leakage Inductance of a Single Rotor Bar [H]
l_a	Machine Active Length [m]
l_{bar}	Rotor Bar Length [m]
l_{ew}	Average Length of Stator End Winding [m]
L_{ew}	Leakage Inductance of a Single Rotor Bar [H]
L_{mT}	T-Model Magnetizing Inductance [H]
$L_{r\lambda,r}$	Rotor Leakage Inductance [H]
$L_{r\lambda}$	T-Model Rotor Leakage Inductance [H]
$L_{s\lambda,ew}$	Stator End Winding Leakage Inductance [H]
$L_{s\lambda,slot}$	Stator Slot Leakage Inductance [H]
$L_{s\lambda}$	T-Model Stator Inductance [H]
L_{scr}	Short Circuit Ring Inductance [H]
l_s	Equivalent Length of Stator [m]

n	Rotor Speed [rpm]
n_{max}	Maximum Rotor Speed [rpm]
N_{ph}	Number of Phases
n_s	Number of stator turns per slot
p	Number of Poles
p_ν	Impedance Transformation factor From Rotor to Stator
P_{airgap}	Airgap Power [W]
P_c	Core Loss [W]
$P_{loss,dq}$	Total Loss from dq Circuit Model [W]
P_{loss}	Total Loss [W]
P_{mech}	Mechanical Power [W]
P_{rb}	Rotor Bar Loss [W]
P_{sw}	Stator Winding Loss [W]
Q	Reactive Power [VAR]
Q_r	Number of Rotor Bars
Q_s	Number of Stator Slots
q_s	Number of slots per pole per phase
R_r	Rotor Resistance in Inverse Gamma Model [Ω]
r_r	Rotor Radius [m]
R_s	Stator Resistance [Ω]
R_{bar}	Resistance of Single Rotor Bar [Ω]
R_s	Stator Resistance [Ω]
R_c	Core Loss Resistance [Ω]
R_d	D-axis Resistance [Ω]
r_{fill}	Stator Slot Fillet Radius [m]
R_q	Q-axis Resistance [Ω]
$R_{r,r}$	Rotor Resistance [Ω]
R_{rT}	T-Model Rotor Resistance [Ω]
$r_{s,out}$	Stator Outer Radius [m]
R_{scr}	Short Circuit Ring Resistance [Ω]
R_{sew}	Stator End Winding Resistance [Ω]
r_{scr}	Short Circuit Average Ring Radius [m]
r_{shaft}	Shaft Radius [m]
s	Slip of the Induction Machine

T	Electromagnetic Torque [Nm]
T_{max}	Maximum Electromagnetic Torque [Nm]
T_{sim}	Maximum Electromagnetic Torque [Nm]
U_m	Magnetising Voltage Magnitude [V]
U_s	Stator Voltage Magnitude [V]
U_{DC}	DC-Link Voltage Magnitude [V]
U_{LL}	Line to Line Voltage Magnitude [V]
$U_{s,max}$	Maximum Stator Voltage [V]
u_{sq}	Stator Voltage in d-direction [V]
u_{sd}	Stator Voltage in q-direction [V]
w_{ew}	Stator End Winding Width [m]
w_{r0}	Rotor Slot Opening Width [m]
w_{r1}	Rotor Slot Outer Width [m]
w_{r2}	Rotor Slot Inner Width [m]
w_{s0}	Stator Slot Opening Width [m]
w_{s1}	Stator Slot Outer Width [m]
w_{s2}	Stator Slot Inner Width [m]

Contents

1
Introduction

An induction motor operates based on the principle of induced current in the rotor through the interaction with rotating magnetic fields created by the stator windings, which generates the necessary torque to rotate the rotor. Induction machines are one of the most popular machines in the world due to their high efficiency, robustness and ease of manufacturing. Their application varies from from household appliances to industrial application. They are gaining popularity in electric vehicle application as they can provide a more sustainable alternative to PMSM.

This thesis compares the IM designed for EV application in regards to tooth forces, torque ripple and losses when it is excited with purely sinusoidal feeding and PWM feeding.

1.1 Background

As the world is transitioning from fossil fuels to clean and sustainable energy systems, there has been a rise of electric vehicles sold around the world. A critical aspect in the selection of electric motors is the sustainability of all its individual components, and induction machines have an advantage in this regard as compared to PMSM. The lack of magnets in an induction machine makes it so that all the components in the IM can be more easily recycled and reused at the end of the machine's life. As the materials used in PMSM, mainly rare earth metals used in the magnets, are such that they poses a serious supply risk and are mined in places which are known to have risk of human rights violation and conflict zones in the world, the IM can be a very good choice as the world of EV grows with the time. Furthermore, the design of the induction machine is simpler and more robust, making them more reliable and less prone to failure compared to PMSM.

1.2 Aim

There are two main objectives of this thesis. The main one is to employ PWM feeding and purely sinusoidal feeding and compare the tooth forces, torque ripple and losses in the induction machine. The other one is to employ a minimum loss control algorithm for the IM.

1.3 Problem Definition

It is commonly acknowledged that while no model can accurately reflect all aspects of a complex system such as electric motors, certain models can still provide valuable insights. As our study is concerned with the minimum loss control and calculation of losses in the motor, the selected model of the IM should be able to account for as many losses as possible. However, the model should also provide us a simpler way to implement our control algorithms. The inverse gamma model could be one of the possible models as it is easy to implement control algorithms. However, as the typical inverse gamma model does not include core losses, we have to modify the model to accommodate the core losses in the motor.

In addition, the parameter by which we model our IM must be found. Analytical approach may be used to get the approximate values i.e to perform calculations by hand based on the available dimensions of the motor. Ansys Maxwell, which is a FEM software that can also be used as a tool to model our IM. No Load Test and Locked Rotor test can be performed from which we can extract the information about our model parameters. With the help of ANSYS Maxwell we can also analyze the current and frequency dependency of our model parameters.

A system to feed the IM with PWM also needs to be developed for our work. This can be done with the help of for example MATLAB.

After all these have been set, the performance of the IM model is compared on the basis of tooth forces, torque ripple and losses when it is fed with the purely sinusoidal input and PWM input.

1.4 Scope

The circuit model of the IM which was selected and used for the steady state minimum loss control which takes into account the resistive losses in the stator and rotor bars. The typical inverse gamma model was modified in such a way that it could account for core losses which is further explained in chapter 2.4. Mechanical losses and other extra losses were neglected.

The minimum loss control algorithm only controls the steady state reference of the IM. So, no transients are taken into account for the loss calculation. Similarly, the losses from outside of the induction machine like in the inverter, cables, etc were neglected.

The IM model implemented in Maxwell Ansys only focuses on the electromagnetic aspect of the machine, so thermal aspects were not taken into consideration.

2
Theory

The induction motor (IM), invented by Nikola Tesla, is one of the most commonly used electrical motors worldwide due to its affordability and robustness. The IM can be classified into two types, namely squirrel cage IM and wound rotor IM, based on the type of rotor used. For our thesis work, we have chosen the squirrel cage IM due to its simplicity in construction. The longitudinal conductive bars of the rotor are made up of aluminum and are connected at both ends by a short circuit ring. The stator, made up of laminated steel with slots and teeth, surrounds the rotor, and the slots are filled with copper windings.

2.1 Tooth Force

In the design process of electrical machines it is important to know the distribution of electromagnetic force density. The force may cause structural deformation and this kind of deformation can lead to problems such as mechanical vibrations and noises. The force can be decomposed into tangential and radial components. It is the tangential forces in the air gap between the surface of the stator teeth and the rotor which are responsible for torque production in the machine. However, it is the radial component of the force along the length of the stator tooth that contributes to the noise and vibration of the stator structure[1].

Using Maxwell Stress Tensor Method, the radial and tangential force density acting on a stator tooth can be expressed as [2]

$$f_r = \frac{B_r^2 - B_t^2}{2\mu_0} \tag{2.1}$$

$$f_t = \frac{B_r B_t}{\mu_0} \tag{2.2}$$

where, f_r is the radial component of force density(N/m^2), f_t is the tangential component of force density(N/m^2), B_r is the radial component of magnetic flux density and B_t is the tangential component of magnetic flux density.

The magnitude of tooth forces is dependent on a number of factors, including the number of stator and rotor teeth, the air gap between the stator and rotor, and other electrical and mechanical properties of the machine. In general, machines with higher numbers of teeth

will experience larger tooth forces, as will machines with larger air gaps[3].

The tooth forces can cause mechanical stress on the rotor and stator teeth. It can also lead to unwanted vibration and noise in the machine. It is important to design induction machines with appropriate rotor and stator teeth configurations to get proper tooth force and ensure smooth and reliable operation.

2.2 PWM Feeding

PWM is a modulation technique in which the average value of voltage (and current) fed to the load is controlled by turning the switch between supply and load on and off at a fast rate. Three-phase bipolar Pulse Width Modulation (PWM) is one of the commonly used method for controlling the speed and direction of three-phase AC motors. This technique involves generating high frequency pulses to regulate the amount of power delivered to the motor.

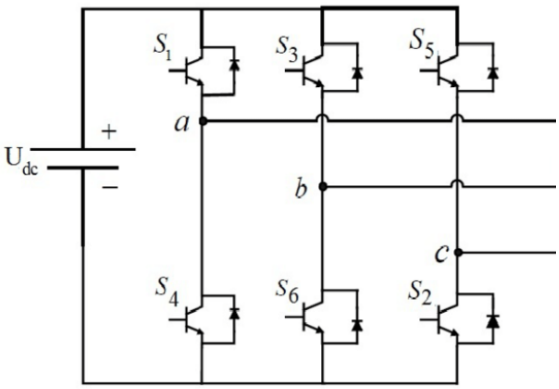

Figure 2.1: Pulse Width Modulation

To generate a PWM signal, a reference waveform, in this case a triangular waveform is compared with a variable-width signal, which is derived from a DC voltage source. The resulting signal is then used to selectively turn on and off the high-side and low-side switches of each pair of switches that control the amplitude and phase of the voltage delivered to the motor.

One of the main advantages of PWM is its efficiency. In other voltage control methods, such as linear voltage regulators, the energy is wasted as heat, resulting in lower efficiency. However, in PWM the switches used to control the voltage is either fully on or fully off and this method of switching allows for the minimum power dissipation in the devices. This means that the efficiency of the system is very high, which is important in applications where energy efficiency is a priority, such as EVs.

However, there are also some disadvantages with PWM. One of these is that it can produce high-frequency noise, which can interfere with other electronic devices. The high-frequency switching of the power electronic device can cause electromagnetic interfer-

ence (EMI), which can be problematic in some applications [4].

In a nutshell, by controlling the average voltage delivered to the motor, three-phase bipolar PWM provides precise control of the motor's speed and excitation while minimizing losses in the motor and the power electronics. It is also a relatively simple and cost-effective way to control three-phase AC motors.

2.3 T-Model and Estimation of Parameters

The three phase induction machine can be represented as a equivalent electric circuit model for each phase as shown in figure 2.2.

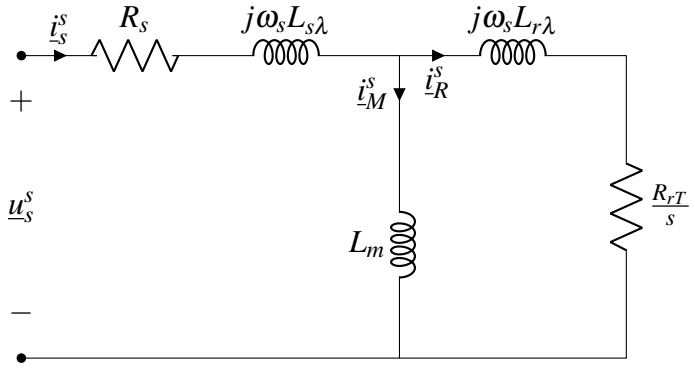

Figure 2.2: T-model circuit

Based on the geometry of the IM, a rough estimation of the parameter can be made. The method and the empirical formulas used to estimate these parameters were taken from [5].

The stator winding resistance R_s can be calculated as

$$R_s = \frac{2q_s n_s \rho_{cu}(l_{ew} + l_a)}{c_s A_{cond}} \tag{2.3}$$

where q_s is the number of slots per pole per phase , n_s is the number of turns per slot , ρ is the density of the copper, l_{ew} is the length of the end winding , l_a is the active length of the machine, c_s is the number of parallel branches and A_{cond} is the cross section area of the conductor.

As we know, the rotor of IM can be divided in two parts i.e rotor bars and short circuit rings. So, the resistance of the rotor can be calculated by summing the individual resistances of these two parts.

The resistance of short circuit ring R_{scr} can be calculated as

$$R_{scr} = \frac{2\pi \rho_{al} r_{scr}}{Q_r A_{scr}} \tag{2.4}$$

where ρ_{al} is the density of aluminium, Q_r is the number of rotor bars, A_{scr} is the cross section area of the short circuit ring and r_{scr} is the radius of short circuit ring. Similarly, the resistance of rotor bars given by

$$R_{bar} = \frac{2\rho_{al} l_a}{A_{r,slot}} \tag{2.5}$$

where $A_{r,slot}$ is the rotor slot area.

So, the total resistance of the rotor on the rotor side can be written as

$$R_r^r = R_{bar} + 2R_{scr}\left(\frac{Q_r}{\pi p}\right)^2 \tag{2.6}$$

R_r^r can be transformed to the stator side by multiplying it with

$$p_v = \frac{N_{ph} n_s^2 q_s^2 k_1^2 p^2}{Q_r C_s^2} \tag{2.7}$$

Finally, the rotor resistance on stator side can be expressed as

$$R_r^s = p_v R_r^r \tag{2.8}$$

The magnetising inductance L_m can be calculated as

$$L_m = \frac{6\mu_0 n_s^2 q_s^2 k_1^2 l_a r_r}{\pi c_s^2 h_{gap}} \tag{2.9}$$

where h_{gap} is an equivalent air gap length , r_r is the rotor radius and k_1 is the winding factor for the fundamental frequency which is calcaulated as

$$k_1 = \frac{sin(\pi/6)}{q_s sin(\pi/6q_s)} cos(\frac{\gamma_p p}{2}) \tag{2.10}$$

where γ_p is the winding pitch factor.

Similarly, the stator leakage inductance can be calculated as the summation of the stator slot leakage inductance and the end winding leakage inductance. Initially, the stator slot leakage inductance $L_{s\lambda,slot}$ can be estimated as

$$L_{s\lambda,slot} = \frac{\mu_0 n_s^2 q_s^2 l_a p}{3c_s^2}\left(\frac{2(h_{s1}+h_{s2}+r_{fill}}{w_{s1}+w_{s2}} + \frac{3h_{s0}}{w_{s0}}\right) \tag{2.11}$$

where μ_0 is the permeability of vacuum. The end winding leakage inductance can be calculated as

$$L_{s\lambda,ew} = \frac{Q_s}{N_{ph}} q_s \left(\frac{n_s}{c_s}\right)^2 \mu_0 l_{ew} \lambda_w \tag{2.12}$$

where,

$$l_{ew}\lambda_w = 2h_{ew}\lambda_{hew} + w_{ew}\lambda_{wew} \tag{2.13}$$

l_{ew} and w_{ew} are the length and width of the end winding. λ_{lew} and λ_{wew} are empirically determined factors which can be found in [6].

2.4 Inverse Gamma Model

To more easily get the parameters of the equivalent circuit and control the steady state of the machine the T-model can be simplified even more by converting it to the so called inverse gamma model[7]. This conversion makes a combination of the stator and rotor inductance into one new inductance of the stator L_σ reducing the number of parameters in the control model and simplifies calculations. An additional resistance R_c is added to the stator part of the circuit model of the standard inverse gamma model in order to represent the core losses of the machine.

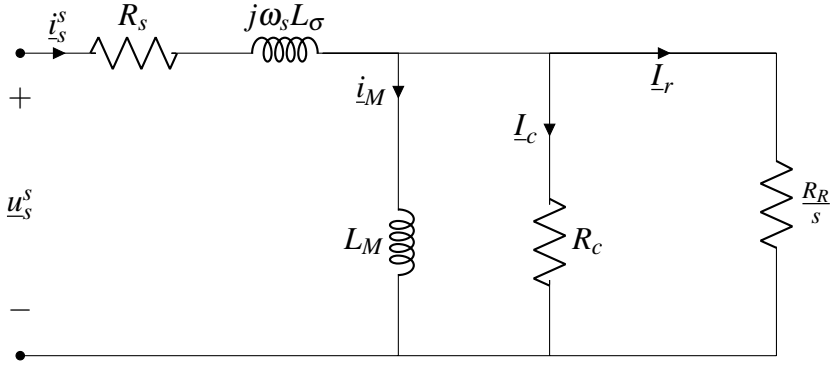

Figure 2.3: Inverse gamma model circuit

Assuming that the dq-component of the current always is perfectly aligned with the magnetising current i_M and modelling the rotor as two parts, one part resistor and a second part as a voltage source representing the back EMF of the machine. That gives the circuit model in figure 2.4 below

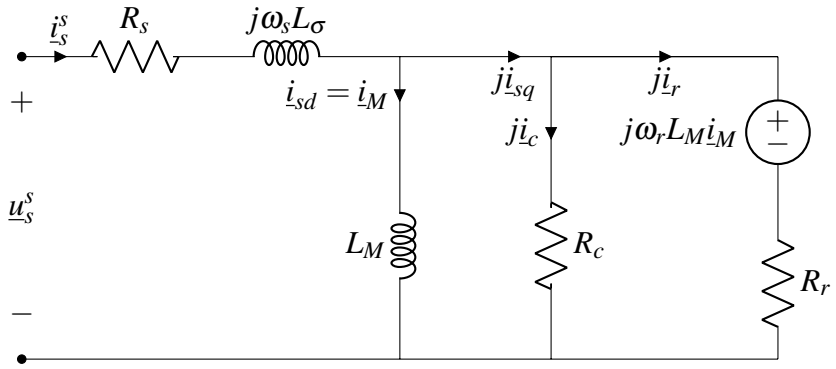

Figure 2.4: Inverse gamma model circuit with dq-quantities and rotor modeled as resistance and back EMF

2.4.1 Converting to inverse gamma model

The new parameters in inverse gamma form explained by [8] can be expressed as

$$L_s = L_{s\lambda} + L_m \tag{2.14}$$

$$L_r = L_{r\lambda} + L_m \tag{2.15}$$

$$L_M = \frac{L_m^2}{L_r} \tag{2.16}$$

$$L_\sigma = L_s - L_M \tag{2.17}$$

$$R_R = \left(\frac{L_m}{L_r}\right)^2 R_r \tag{2.18}$$

2.4.2 Equations of inverse gamma

For the inverse gamma model where the flux is modeled as flux linkage then voltages can be expressed as

$$u_{sd} = L_\sigma \frac{di_{sd}}{dt} + (R_s + R_R)i_{sd} - \omega_s L_\sigma i_{sq} - \frac{R_R}{L_M}\Psi_r \tag{2.19}$$

$$u_{sq} = L_\sigma \frac{di_{sd}}{dt} + (R_s + R_R)i_{sq} + \omega_s L_\sigma i_{sd} + \omega_r \Psi_r \tag{2.20}$$

Where the rotor flux linkage Ψ_r is the real component in on the d-axis.

From figure 2.4 the stator voltages are expressed as

$$u_{sd} = R_s i_{sd} - \omega_s L_\sigma i_{sq} \tag{2.21}$$

$$u_{sq} = R_s i_{sq} + \omega_s L_\sigma i_{sd} + \omega_s L_M i_{sd} \tag{2.22}$$

The stator voltage u_s and the amplitude of that stator voltage U_s given the dq-voltages as

$$\underline{u_s} = u_{sd} + j u_{sd} \tag{2.23}$$

$$U_s = \sqrt{u_{sd}^2 + u_{sd}^2} \tag{2.24}$$

The two equations above can be used for the dq-currents as well. The torque of the machine is given by

$$T_e = \frac{3n_p}{2} L_M i_{sd} i_r \tag{2.25}$$

where the rotor current can be expressed as

$$i_r = \frac{R_c}{R_c + R_r} i_{sq} - \omega_r \frac{L_m}{R_c + R_r} i_{sd} \tag{2.26}$$

where the relationship between the stator and rotor frequencies in the circuit model is given by

$$\omega_r = \omega_s - \frac{R_R i_r}{L_M + i_{sd}} \tag{2.27}$$

2.5 Locked rotor & No load test

To get the parameters for the inductance and rotor resistance in the inverse gamma model several locked rotor and no load tests were run. The equivalent circuit can be reduced while running the two test so that the individual parameter can be assumed

2.5.1 Locked rotor test

The locked rotor test is done in simulation by putting the slip term equal to one making the rotor stationary but the stator are still supplied with current and voltage. As the slip is equal to one the equivalent rotor part of the circuit in figure 2.3 becomes only R_R and it can be assumed that very little or no current goes through the magnetising inductance L_M and core loss resistance R_C as they have much greater resistance in the equivalent circuit. Reducing the circuit diagram to as in figure 2.5

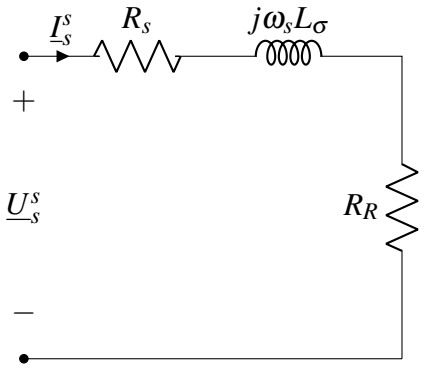

Figure 2.5: Locked rotor test circuit model

2.5.2 Locked rotor parameter calculation

Then using the reduced circuit for the locked rotor test and the jω-method one can calculate the stator inductance L_σ with

$$L_\sigma = \frac{Q}{\omega_s(I_{sa}^2 + I_{sb}^2 + I_{sc}^2)} \tag{2.28}$$

where Q is the total reactive power ω_s the stator frequency and I_s currents for each phase.

2.5.3 No load test

The slip for the no load test is the opposite to the locked rotor test as the slip now is equal to zero meaning that no load is applied to the rotor shaft. Making the stator frequency ω_s and rotor frequency ω_r equal. This reduces the equivalent circuit diagram to figure 2.6 as it can be assumed that no current goes through the rotor resistance R_R branch as that resistance now theoretically goes towards infinity.

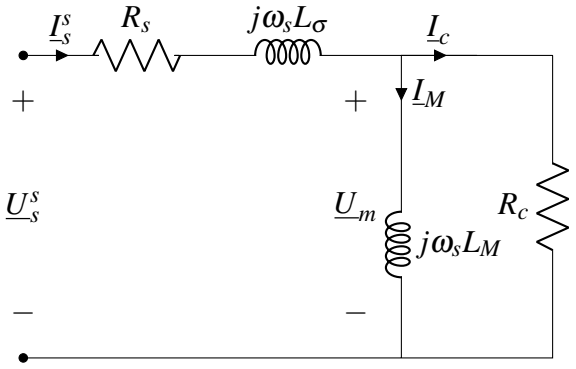

Figure 2.6: No load test circuit model

2.5.4 No load parameter calculation

The parameters calculated with the results from a no load test is the magnetising inductance L_M and the core resistance R_c. The voltage over these two parameters can be found using KVL. As the inductance's of the circuit model are assumed to be ideal and do not consume any active power the active power loss of the core is then the difference between the total active power in to the machine and the loss from the stator resistance.

$$U_m = U_s - j\omega_s L_\sigma I_s - R_s I_s \tag{2.29}$$

The core resistance R_c can be calculated using the magnetising voltage U_m and the active core loss P_c during no load. The core loss can also be taken from simulations

$$P_c = P_{in} - R_s I_s^2 \tag{2.30}$$

$$R_c = \frac{|U_{ma}|^2 + |U_{mb}|^2 + |U_{mc}|^2}{P_c} \tag{2.31}$$

The magnetising inductance can be calculated from the total reactive power of the machine during no load, the impedance of the inductance L_σ calculated from the locked rotor test results and with the frequency and current of the magnetising inductance

$$L_M = \frac{Q - \omega_s L_\sigma (I_{sa}^2 + I_{sb}^2 + I_{sc}^2)}{\omega_s (I_{ma}^2 + I_{mb}^2 + I_{mc}^2)} \tag{2.32}$$

2.6 Loss estimation & control

To more accurately evaluate the losses it can be separated into different section depending on that cause that component of the total loss such as core loss and resistive losses from the stator windings

$$P_{loss} = P_{sw} + P_{rb} + P_{core} = R_s \left(i_{sd}^2 + i_{sq}^2\right) + R_r i_r^2 + R_c \left(i_{sq}^2 - i_r^2\right) \tag{2.33}$$

where the rotor current is given by (2.26).

The power loss can then finally be expressed as

$$P_{loss,dq} = R_d i_{sd}^2 + R_q i_{sq}^2 \tag{2.34}$$

where the dq-resistances are given by

$$R_d = R_s + \frac{L_m^2}{R_c + R_r} \omega_r^2 \tag{2.35}$$

$$R_q = R_s + \frac{R_c R_r}{R_c + R_r} \tag{2.36}$$

2.6.1 Parameter Mapping

It can be seen in the formulas for leakage inductance (2.28), the magnetising inductance (2.32) and the core resistance (2.31) that the parameters estimated depend on the stator input current and frequency. In order to find the dependency of those quantities the equivalent circuit parameters results are to be taken from a number of locked rotor and no load tests with different input current and frequency.

2.6.2 Torque Speed Curve

To know for what range of i_d & i_q as well as what torque and speed the machine can operate at the current and voltage rating of the machine must be taken into consideration. This range of operation will be given by the so called MTPA curve with different regions depending on the limiting factor for that specific range of operation. The first region is linear as the increase in torque in relation to increase in speed can be achieved by increasing the current amplitude being feed to the machine. The limiting factor is then the current amplitude, given maximum torque per ampere. Then as the current can not be increased further the machine will be at its so called base speed or synchronous speed and the stator voltage will be at its max and equal to the back EMF. Field weakening should be used to decrease the back EMF to be able to increase the speed of the machine further. Then at a certain speed the rotor frequency will need a voltage higher than the max voltage of operation that field weakening can achieved and then the Voltage amplitude is the limiting factor, Maximum Torque per Voltage (MTPV).

$$U_{s,max} = \frac{U_{DC}}{\sqrt{3}} \tag{2.37}$$

With the assumption that the rotor flux is orientated in the d-current direction at all times then the following expression can be used instead of (2.25).

$$T_e = \frac{3n_p}{2} L_M i_{sd} i_{sq} \tag{2.38}$$

2.6.2.1 MTPA operation

The angle between the dq-currents resulting in the maximum torque is to be found. Using (2.21) and (2.22) for the currents and using the relations(2.23) and (2.24) using Euler's formula to get it dependent on angle inserting it in (2.38). Where the d-current becomes the cosine part while the q-current the sine part this gives the following expression for the torque.

$$T_e = \frac{3n_p}{2} L_M I_s^2 cos(\theta) sin(\theta) \tag{2.39}$$

The maximum torque of (2.39) is given by the derivative by angle equal to zero as

$$\frac{dT_e}{d\theta} = 0 \tag{2.40}$$

This gives a maximum torque at $\theta_{max,Te} = 45^\circ$ dq-current angle.

2.6.2.2 Field weakening operation

As explained above at the base speed the machine will be at a the maximum stator voltage and a field weakening scheme need to be used to decrease the d-axis flux to increase the speed further[9]. This speed can be expressed as

$$\omega_{base} = \frac{U_{s,max}}{\sqrt{(L_\sigma^2 + (L_\sigma + L_M)^2) I_{s,max}^2 cos(\theta_{max,Te})^2}} \tag{2.41}$$

where the angle who gives the maximum torque $\theta_{max,Te}$ is used as well as the maximum stator voltage and current of the machine.

The currents during field weakening can be expressed by

$$i_{sd} = \sqrt{\frac{U_{s,max}^2 - I_{s,max}^2 L_\sigma^2 \omega_s^2}{L_M(L_M + 2L_\sigma)\omega_s^2}} \tag{2.42}$$

$$i_{sq} = \sqrt{I_{s,max} - i_{sd}^2} \tag{2.43}$$

Simplifying equations (2.19) and (2.20) by assuming the slip for high speed of field weakening at steady state is so small that $\omega_r \approx \omega_s$ that the voltages can be simplified to

$$u_{sd} = \omega_s L_\sigma i_{sq} \tag{2.44}$$

$$u_{sq} = \omega_s i_{sd}(L_\sigma + L_M) \tag{2.45}$$

2.6.2.3 MTPV operation

At a certain speed of operation of the machine will reach its max slip frequency and in order to not make the operation unstable the control scheme is changed to maximum torque per voltage(MTPV). This region of operation is derived by finding the voltage angle in dq-domain that gives that maximum torque but also within previously mentioned limits of operation. This is done by putting (2.44) and (2.45) into (2.38) which gives

$$T_e = \frac{3n_p L_M U_{smax}^2}{2\omega_s^2 L_\sigma (L_\sigma + L_M)} cos(\theta) sin(\theta) \tag{2.46}$$

With the same procedure as in section2.6.2.1 the maximum angle for this operation range is an angle of 135°, the second maximum of the expression. Inserting that angle of maximum voltage into (2.44) and (2.45)the currents then becomes

$$i_{sd} = \frac{U_{s,max}}{\sqrt{2}\omega_s (L_\sigma + L_M)} \tag{2.47}$$

$$i_{sq} = \frac{U_{s,max}}{\sqrt{2}\omega_s L_\sigma} \tag{2.48}$$

The max slip frequency is given by the currents of the MTPV current equations that intersect with the maximum current of field weakening.

$$\omega_{ms} = \frac{U_{s,max}}{I_{s,max}} \sqrt{\frac{L_\sigma^2 + (L_\sigma + L_M)^2}{2L_\sigma^2 + (L_\sigma + L_M)^2}} \tag{2.49}$$

2.6.3 Loss estimation

The losses of the machine can be described by modeling characterising the losses into different types and then estimating them more correctly. As described earlier in 2.4. The core losses are modeled by a equivalent resistance R_c and the resistive losses of the windings and the rotor bars are modeled by their respective resistances

$$P_{loss} = P_{sw} + P_{rb} + P_{core} = R_s \left(i_{sd}^2 + i_{sq}^2\right) + R_r i_r^2 + R_c \left(i_{sq}^2 - i_r^2\right) \tag{2.50}$$

Where the rotor current is given by (2.26)and frequency by (2.27)

The losses in dq-domain is then given by

$$P_{loss,dq} = R_d i_{sd}^2 + R_q i_{sq}^2 \tag{2.51}$$

where the dq-resistances are expressed as

$$R_d = R_s + \frac{L_m^2}{R_c + R_r} \omega_r^2 \tag{2.52}$$

$$R_q = R_s + \frac{R_c R_r}{R_c + R_r} \tag{2.53}$$

2.6.4 Minimum loss control

The minimum loss control want to minimise the total loss of the machine given the assumptions of equivalent resistances for the core losses for the circuit model in figure 2.4. The purpose of the control is to give the current and stator frequency that make the losses minimal but still achieving the corresponding speed and torque for a given operating point. The algorithm should then minimise the loss function (2.51) while the following constraints are to be meet

- $\omega_r = \omega_{r,op}$
- $T_e = T_{e,op}$
- $I_s =< I_{s,max}$
- $U_s =< U_{s,max}$
- $\omega_s =< \omega_{s,max}$

where op stands for the given operating points torque and speed. A large range of operating points are to be swept. The operating points of torque and speed evaluated are the ones under the MTPA limiting line and under the field weakening limiting line.

3
Case Set-up

The IM was modelled and evaluated using the FEM software ANSYS Maxwell as the solution for electromagnetic field in the complex machine structure was possible and convenient in ANSYS Maxwell. Implementation of PWM could be carried out with Simplorer or Matlab. However, it was more convenient and less time consuming when implemented in Matlab. Similarly, Matlab was also used to employ minimum loss control algorithm with the help of data obtained from ANSYS Maxwell.

3.1 Simulation Set-up in Ansys Maxwell

Modelling and simulation of the concerned IM was carried out with the following assumptions.

- All the simulations were carried out in 2D to simplify the machine model.
- Symmetry was used to reduce the model to be as small as possible size in order to save computational time without sacrificing accuracy.
- Simulations were carried out using sinusoidal voltage feeding and PWM feeding only.
- The core material was set to be M235-35A. The BH curve and core loss properties connected to the material is presented in the figure A.1 and A.2 in the Appendix.
- Copper wires were used in the stator winding while rotor bars were set to be aluminium.
- The stator windings were set as stranded.
- The stator resistance was hand calculated and used as input to ANSYS Maxwell for voltage excitation.

3.2 Machine Model

The Audi e-tron IM model was already available to us from the FEM based design of the electrical machines course. The geometry of the machine is shown in figure 3.1. The various details regarding the dimension of the machine as well as the information regarding the coil is given in table 3.1

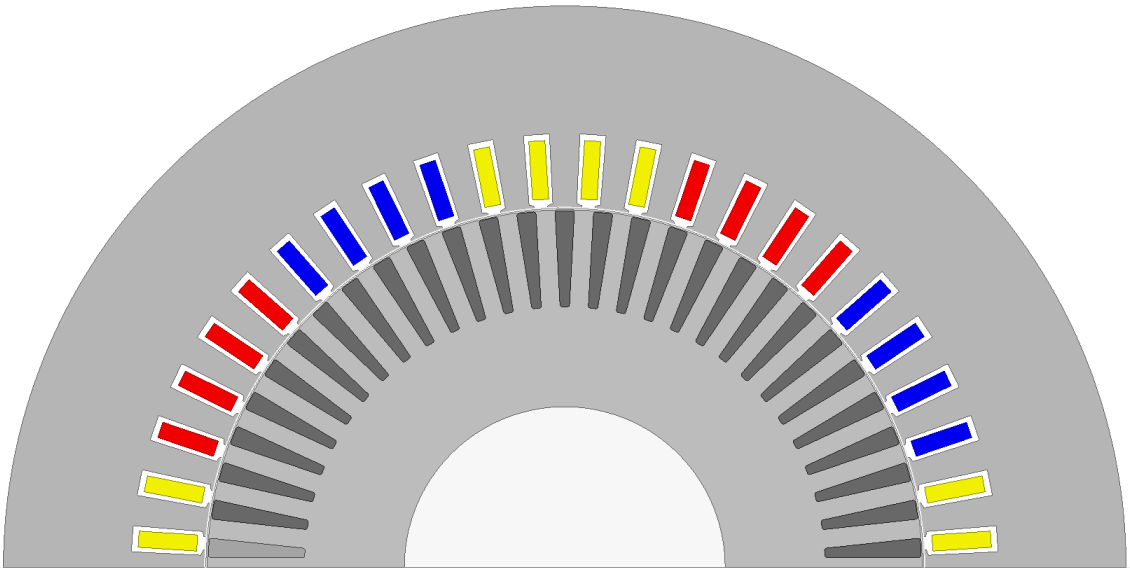

Figure 3.1: ANSYS Maxwell model of the investigated IM

Table 3.1: Motor Parameters

Description	Parameter	Value	Unit
Stator coil material	-	Copper	-
Rotor bar material	-	Aluminium	-
Iron core material	-	M235-35A	-
Phases	N_{ph}	3	-
Pole Pairs	n_p	2	-
Number of stator slots	Q_s	48	-
Number of rotor slots	Q_r	58	-
Number of slots per pole per phase	q_s	4	-
Iron core stack length	l_a	210	mm
Stator outer diameter	d_{so}	245	mm
Stator inner diameter	d_{si}	157.2	mm
Airgap length	l_{gap}	0.6	mm
Rotor outer diameter	d_{ro}	156	mm
Rotor inner diameter	d_{ri}	50	mm
Stator slot opening height	$h_{s0,s}$	0.2	mm
Stator slot wedge height	$h_{s1,s}$	0.4	mm
Stator slot body height	$h_{s2,s}$	15	mm
Stator slot opening width	$b_{s0,s}$	2.9	mm
Stator slot wedge maximum width	$b_{s1,s}$	5.2	mm
Stator slot body bottom width	$h_{s2,s}$	5.7	mm
Radius of stator slot bottom	$r_{s,s}$	0.2	mm
Rotor slot opening height	$h_{s0,r}$	0.2	mm
Rotor slot wedge height	$h_{s1,r}$	0.5	mm
Rotor slot body height	$h_{s2,r}$	20	mm
Rotor slot opening width	$b_{s0,r}$	0	mm
Rotor slot wedge maximum width	$b_{s1,r}$	4.2	mm
Rotor slot body bottom width	$h_{s2,r}$	2.1	mm
Radius of rotor slot bottom	$r_{s,r}$	0.5	mm
Wire cross sectional area	a_{wire}	0.7	mm^2

3.3 Tooth Force Calculation Set up

The radial and tangential force acting on the tooth were studied at five different parts as shown in figure 3.2. Polyline 1 traces the contour of the edge of a single tooth while polyline 2 and polyline 3 lie in the middle and upper part of the tooth respectively as shown in figure 3.2a. Polyline 4 is drawn in such a way that it extends from the midpoint of one slot to the midpoint of another slot with single tooth enclosed as it can seen in figure 3.2b. Finally, polyline 5 extends from the midpoint of one slot to the midpoint of another slot but encloses two teeth as shown in figure 3.2c .

(a) (b)

(c)

Figure 3.2: Location of polylines for tooth force study

3.4 Meshing

The accuracy of a finite element model using ANSYS Maxwell is greatly influenced by the quality of the mesh. The default mesh suggested by ANSYS Maxwell is often too coarse, and as a result, the expected accuracy is difficult to obtain. Therefore, it is necessary to redefine the mesh to ensure the accuracy of the simulation. However, there is no unique solution to this problem, and engineers must judge the mesh to be reasonable based on their experience.

To address this, a meshing strategy was implemented for the FEM model in this study. Figure 3.3 displays the mesh setup utilized in the simulation, while a detailed view of the mesh around the airgap and a tooth is shown in figure 3.4. The mesh was refined in areas of interest to increase the accuracy of the simulation results, particularly in areas where there is significant variation in the magnetic field.

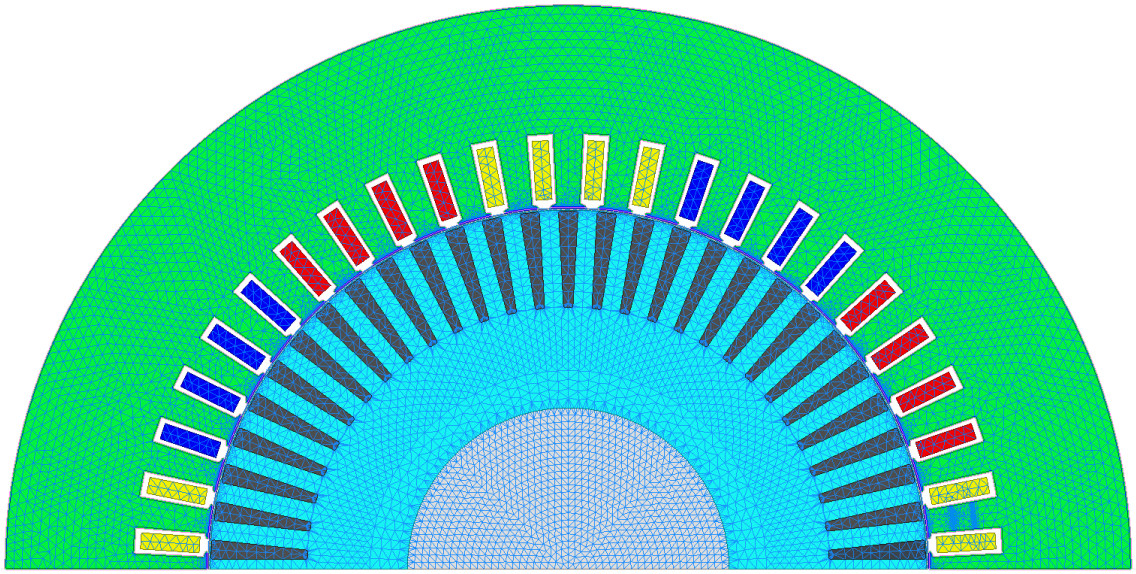

Figure 3.3: ANSYS Maxwell model of the IM with mesh

The type and size of mesh element used on different parts of the machine is shown in the table 3.2

Table 3.2: Meshing

Region	Mesh Type	Mesh Size
Stator	length based	3mm
Coils	length based	3mm
Rotor	length based	3mm
Rotor Bar	length based	3mm
Polyline 1	length based	0.01mm
Polyline 2	length based	0.01mm
Polyline 3	length based	0.01mm
Polyline 4	length based	0.01mm
Polyline 5	length based	0.01mm
Airgap line	length based	0.01mm

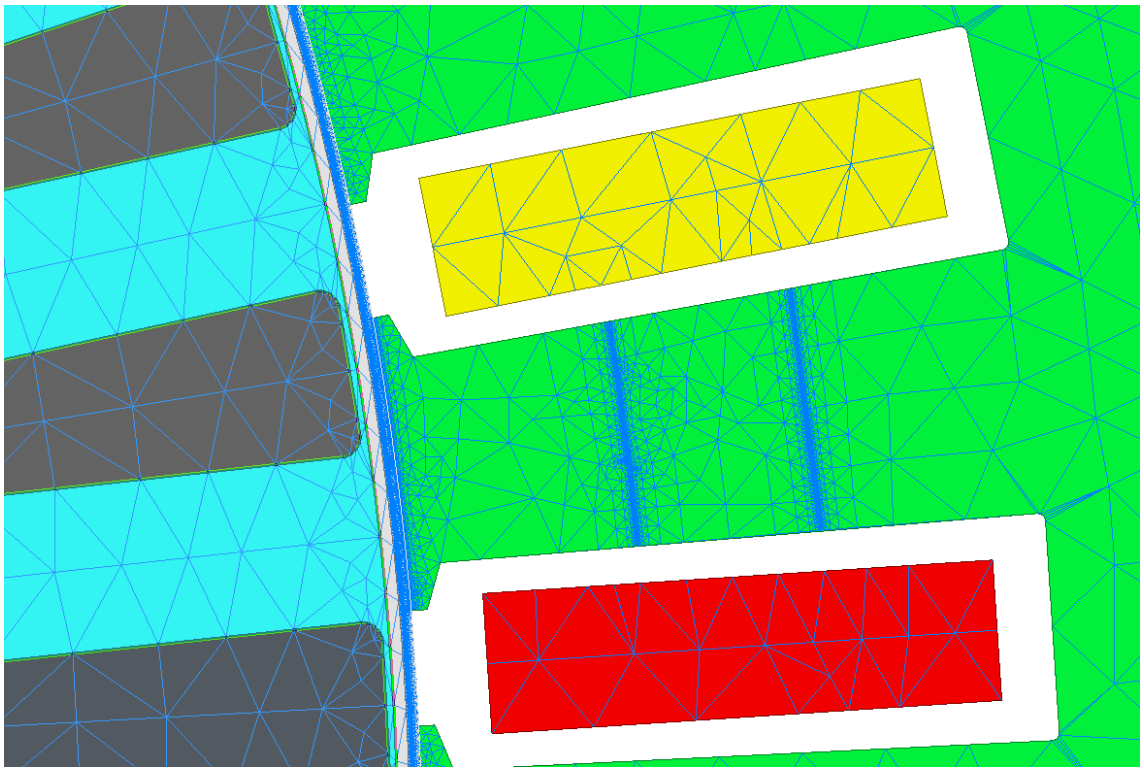

Figure 3.4: Maxwell model of the IM with closer look at the mesh

Overall, the meshing strategy employed in this study was critical to ensure the accuracy of the results from FEM model using ANSYS Maxwell. By refining the mesh in areas of interest, the expected accuracy was achieved with good simulation speed.

3.5 Parameter Estimation from Maxwell Model

3.5.1 Estimation of leakage inductance L_σ and rotor resistance R_r

The leakage inductance L_σ and the rotor resistance were determined with the help of a locked rotor test. The details of this test to determine the motor parameters are already discussed in the section 2.5.1. Even though, the value of L_σ is dependent on the stator current, a current value 250A, was applied at a frequency of 12.5 Hz with slip of 1 which would provide a good estimation of the leakage inductance which was obtained using 2.28. The stator current and frequency dependence of the of the L_σ is discussed more in the upcoming chapter 5.1.1.

As for the rotor resistance R_r, it was calculated using the stator current and the active power during locked rotor test with the following formula

$$R_r = \frac{P}{(I_{sa}^2 + I_{sb}^2 + I_{sc}^2)} \tag{3.1}$$

3.5.2 Estimation of magnetizing inductance and core resistance

The magnetising inductance L_m and the core loss resistance R_c were determined through no load test. A rated current of 250A at rated frequency of 50Hz at 0 slip was applied on the stator. The details regarding the no load test are explained in section 2.5.3. The value of The magnetising inductance L_m and the core loss resistance R_c were estimated using (2.32) and (2.31) respectively. However, it is noteworthy to mention that the magnetizing inductance L_m core loss resistance R_c are dependent on the stator current and frequency which is further explained in sections 5.1.2 and 5.1.3.

3.6 Excitation Sequence in ANSYS Maxwell

A series of simulation sequences were carried out in order to obtain the parameters which enabled us to implement PWM excitation correctly . The simulation sequences is shown in the table below and described in subsequent sections. This method of simulation of sequence was inspired by the article [7].

Table 3.3: Simulation sequence used in ANSYS Maxwell

Simulation step	Description
1	Sinusoidal Current Excitation
2	Sinusoidal Voltage Excitation
3	PWM Voltage Excitation

Step 1

In this step, the stator windings were excited by a purely sinusoidal current and the information on phase current, phase angle and copper losses were obtained.

Step 2

In this step, a voltage excitation was provided to the stator windings based on the information obtained from the step 1. The magnitude of the induced voltage was used and added with the resistive and inductive voltage drop in order to obtain the voltage reference. The phase error due to the derivative of the flux linkage was also compensated.

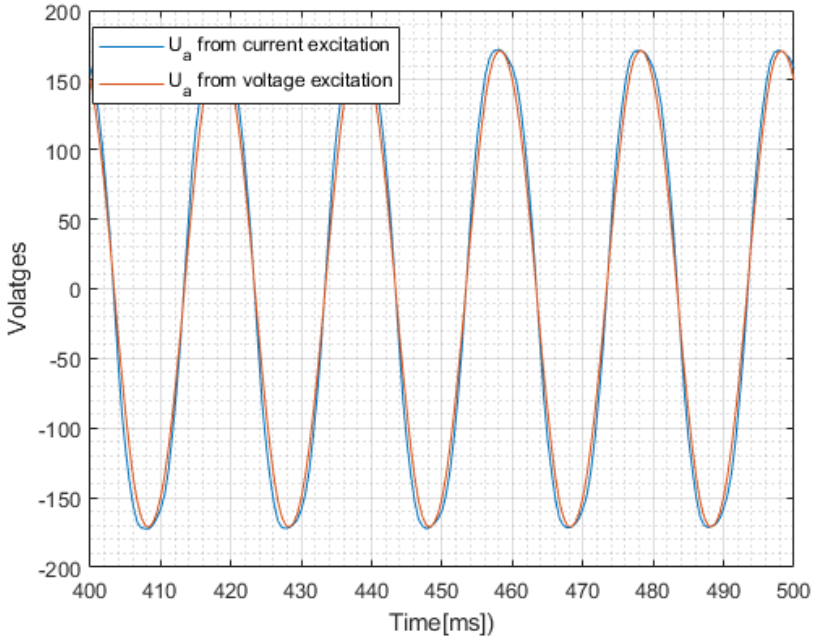

Figure 3.5: Comparison of phase A induced voltage from current and voltage excitation

A comparison of induced voltage waveform in an induction machine when excited with sinusoidal current and sinusoidal voltage can be seen in figure 3.5 . The comparison revealed that while the magnitude and phase of the induced voltage perfectly matched, the waveforms did not overlap perfectly. This discrepancy can be attributed to the difference in the non-uniform current distribution caused by the change in excitation method. When the induction machine is excited by a sinusoidal current, the current is distributed uniformly throughout the windings, resulting in a uniform magnetic field distribution inside the machine. On the other hand, when the machine is excited with a sinusoidal voltage, the current distribution is non-uniform due to the impedance of the machine and the voltage source. This non-uniform current distribution can result in a non-uniform magnetic field distribution inside the machine, which can affect the induced voltage waveform.

Step 3

The results of the phase current, induced voltage and flux linkage from the previous simulations were used to define a set of sinusoidal phase voltage reference vectors. This new set of sinusoidal references is modulated with a triangular wave of frequency 10KHz to generate the pulse width modulation (PWM) patterns, which were subsequently used to excite the machine.

3.7 PWM Implementation

As mentioned in Step 3 of section 3.6 a dataset of the three phase PWM voltages were created in Matlab. Thereafter, it was imported into ANSYS Maxwell which contained the data points for the three phase PWM voltages. In the simulation, a two-step feeding

approach was employed to reduce the time required for the machine to reach a steady state. By initially exciting the machine with a pure sinusoidal voltage waveform, the machine was allowed to reach a steady state quickly. Once the machine has reached this steady state, the excitation is switched to a PWM excitation. This type of excitation technique is illustrated in the figure 3.6.

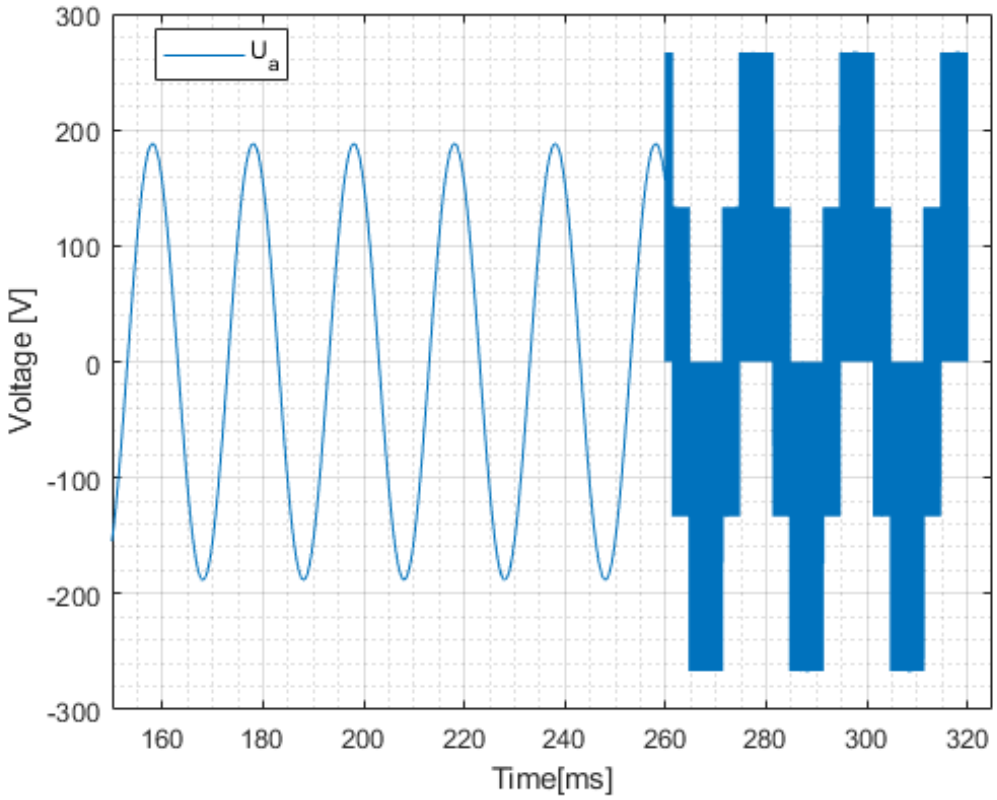

Figure 3.6: PWM Voltage An from Matlab

3.8 Time Step

The accuracy of the simulation results in FEM software such as ANSYS Maxwell is heavily dependent on appropriate meshing and a suitable time step. Experience is crucial in determining the optimal setup for a simulation. As discussed in section 3.4, finer meshing makes simulation time longer. Similarly, a finer time step combined with finer meshing can significantly slow down the simulation process.

Setting the time step for the simulation requires careful consideration. A large time step can result in errors in the simulation output, as data is saved at larger intervals, potentially leading to the loss of valuable information. Conversely, a very small time step can lead to a slow simulation process, significantly increasing the time required to obtain results.

Therefore, it is essential to strike a balance between time step size and simulation speed while ensuring that the results remain accurate. One must exercise caution and take a

strategic approach to determine the optimal time step for their simulation, taking into account factors such as the complexity of the model and the desired level of accuracy.

In case of our simulation, the chosen time step for purely sinusoidal voltage excitation was 0.55 ms whereas, a much finer simulation time of 1μs was used for simulation with PWM feeding as data at very small switching intervals were to to captured. Simulations with different time steps higher and lower than 1μs were also carried to check the viability in regards to accuracy and simulation time.

A simulations with a time step of 0.1μs was initially carried out, but proved to be too fine and resulted in slow simulations and storage issues. A time step of 10μs was also attempted, but the resulting torque as illustrated in figure 3.7 showed significant ripple and failed to capture important data points due to the larger time interval between measurements. Ultimately, a time step of 1μs was selected as an acceptable compromise between accuracy and computational efficiency. The results obtained from this simulation approach will be discussed in the upcoming chapters.

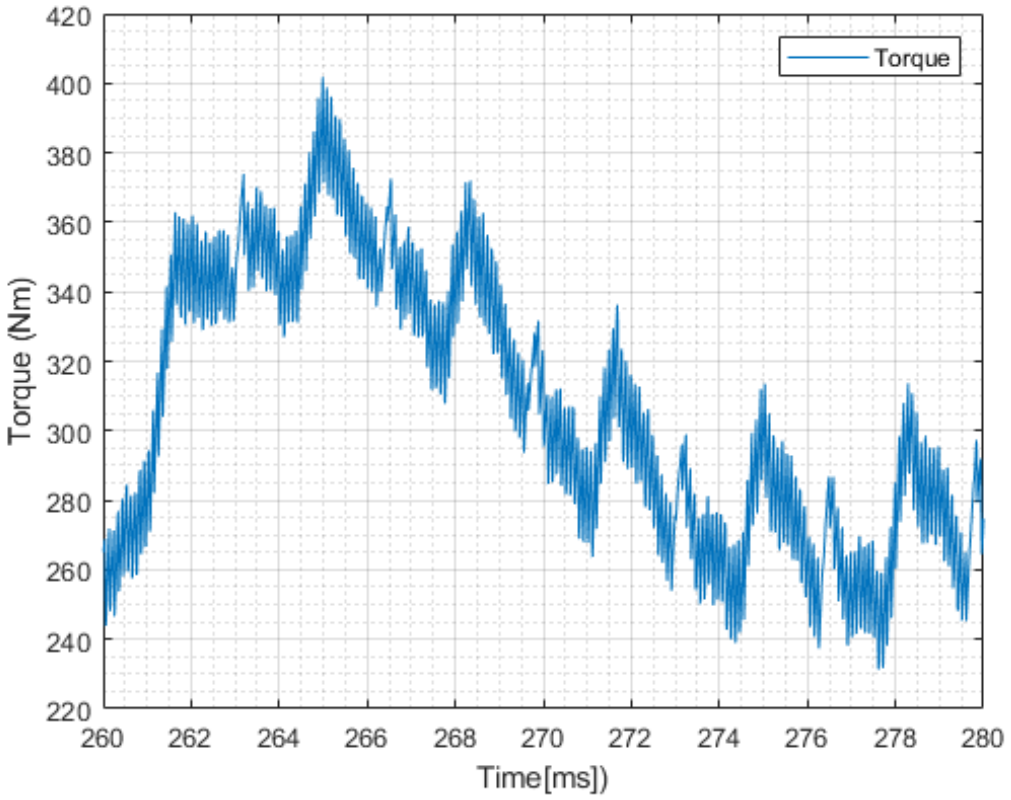

Figure 3.7: Torque with 10μs simulation time step

4

Verification

4.1 Verification of the Model

In order to verify that the motor modelled in ANSYS was a proper representation of the actual machine, parameters obtained from the simulations were compared with the results from analytical calculations.

Table 4.1: Comparison of T-model parameters from simulation and analytical calculations

Description	Parameter	Unit	Simulation	Analytical
Stator Resistance	R_s	Ω	-	0.0652
Rotor Resistance	R_r	Ω	0.0218	0.0215
Magnetising Inductance	L_m	mH	27.3	21.1
Stator Leakage Inductance	$L_{s\lambda}$	mH	0.1799	0.5251
Rotor Leakage Inductance	$L_{r\lambda}$	mH	0.1799	0.23
Core loss Resistance	R_c	Ω	39.88	-

The simulated parameters were found to be closer to the analytical values. The value of stator resistance was analytically calculated. However, it is worth noting that while obtaining the parameters from the locked rotor test, the total leakage inductance was assumed to be equally distributed between the rotor and the stator. The value of stator leakage inductance obtained from the simulation was lower than the analytically calculated value. As the simulation did not include the end winding stator leakage inductance, which may have contributed to the lower value obtained from the simulation. The values from rotor resistance and magnetising inductance from both simulation and analytical calculations are almost the same. In regards to core loss resistance, the value was estimated from simulations only and no analytical calculations were performed.

4.2 Verification of Tooth Force Calculation Setup

Proper simulation set up is essential to obtain tooth force results with higher accuracy. The forces acting on the stator tooth was calculated with Maxwell Stress Tensor formula as discussed in the section 2.1. It is necessary to verify that the technique used in ANSYS Maxwell to obtain the stator tooth force result is accurate.One of the many ways to verify this is to check that the torque obtained from the transient analysis matches the torque estimated using Maxwell Stress Tensor calculation in the field calculator .

Initially, a default meshing of 3 mm was used for every part of the machine. The mesh was also set be 3mm for the airgap arc where the tangential force was calculated which in turn was used to calculate the torque and also to be compared with the torque obtained from the transient analysis. The comparison of the torque obtained with the default meshing of 3mm mesh size is show in figure 4.1.

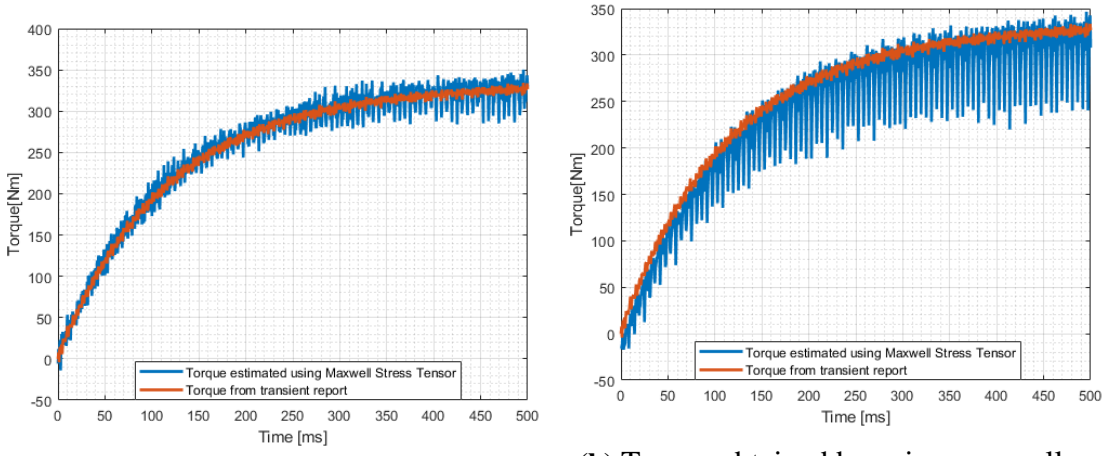

(a) Torque obtained by taking average magnetic flux density first

(b) Torque obtained by using maxwell stress tensor equation first and taking average of tooth force

Figure 4.1: Comparison of electromagnetic torque from ANSYS Maxwell and the estimate based on the surface integral of the tangential force obtained from the Maxwell Stress Tensor calculation with 3mm meshing

From figure 4.1, it can observed that two different results were obtained while using the same formula to calculate the torque in the air gap. First approach was to find the average flux densities in the air gap arc and this average flux densities were used to calculate the tangential force which in turn was multiplied by the active length of the motor and the distance from the center of motor to the arc to obtain the torque. The torque obtained with this calculation sequence is shown in figure 4.1a. However, the second approach was to use the flux densities directly to calculate the tangential force and integrate this tangential force over the length of air gap arc to obtain the average value of tangential force and again multiply by the active length of the motor and the distance from the center of motor to the arc to obtain the torque. The torque thus obtained is shown in figure 4.1b. As it can be noted, the torque obtained with our first approach has less ripple than the torque

obtained using the second approach. One of the reasons for this could be that when we take the average of the flux densities first, the extreme values might have been suppressed and thus giving tangential force with less ripple and ultimately torque with lower ripple than second approach. Hence, one should be observant regarding the calculation sequence while using the field calculator in ANSYS Maxwell.

To accurately calculate the tangential force in the airgap, a high-quality mesh with a fine element size of $0.01mm$ and the first calculation approach described before was used. The tangential force in the airgap was obtained using the fields calculator, which then was multiplied by the model depth and distance from the center to the arc to obtain the torque. To account for the symmetry, a symmetrical multiplier of 2 was used. The resulting torque obtained from the field calculator was compared with the torque obtained directly from the transient report in ANSYS Maxwell. The two torques were found to be perfectly matching, confirming that the tooth force calculation setup was correct. The torques obtained using different techniques are shown in figure 4.2.

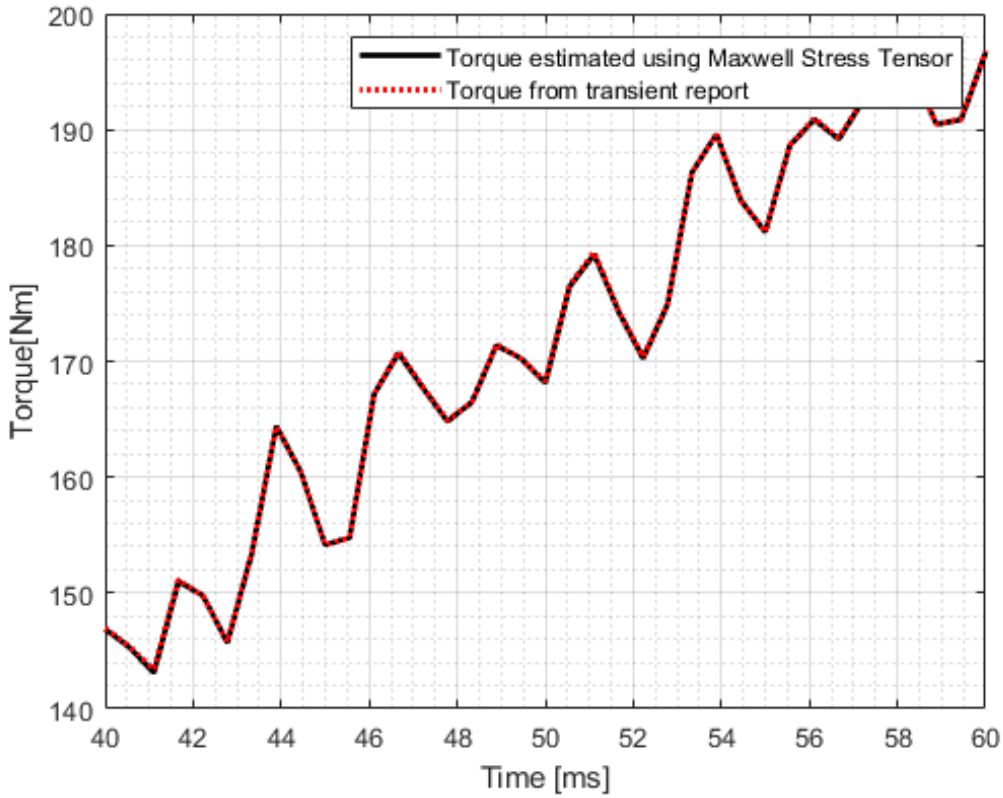

Figure 4.2: Comparison of electromagnetic torque from ANSYS Maxwell and the estimate based on the surface integral of the tangential force obtained from the Maxwell Stress Tensor calculation with 1mm meshing

5
Results

This section presents the results of the thesis work, which covers the impact of stator current on magnestizing and leakage inductance, the effects of frequency and stator current on core less resistance, and a comprehensive comparison of tooth force, torque ripple, and losses under purely sinusoidal voltage versus PWM feeding.

5.1 Parameter Dependency and Minimum Loss Controller

In order to obtain the parameters needed for the minimum loss controller, no-load and locked rotor test were carried out at different current amplitudes and frequencies as explained under section 2.5. The parameters mapping was then used for minimising the function (2.51) using the *fmincon* algorithm in MATLAB with equality and inequality constraints more explained in section 2.6.4. The results of the controller are then compared by losses from using a MTPA controller. The comparison of the two controllers was made with the same limiting line of maximum torque at a specific rotor speed from the MTPA and field weakening, explained under section 2.6.2. It shall be noted that this limiting line is using a constant value estimation of the magnetising inductance taken at simulation results running at a supplied stator frequency of $50Hz$ for the no load test and $12.5Hz$ for the locked rotor test resulting in a limiting line for the controller that is not accurate at different frequencies of operation.

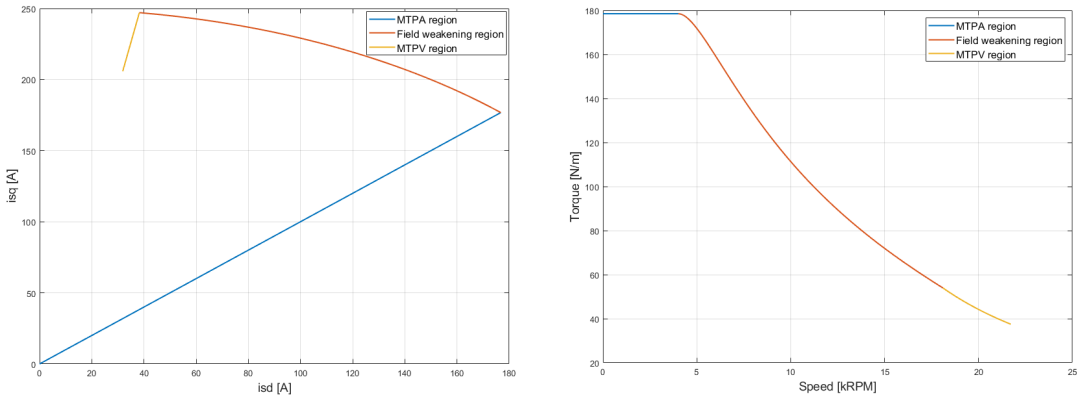

(a) dq-currents operating range

(b) Torque-speed curve limiting line

Figure 5.1: The operating range of the controller expressed in dq-currents quantities and as torque- speed

For the maximum stator current amplitude of 250A and maximum voltage of 800$Vrms$ gives the operating range as is explained in section 2.6.2. The first region of operation is linear and with the angle of 45° as can be seen in 5.1a while the torque is constant in 5.1b. Then at the maximum stator current field weakening scheme is employed and the torque starts to decrease as the speed increase further and at the same time does the d-current component start to decrease compared to the q-current who still increases a little bit. Then at the MTPV region as the speed of the machine increases then the current is reduced as both the d and q-current decreases but the q-component more significantly.

5.1.1 Leakage Inductance

The leakage inductance for different current amplitudes and stator frequencies was determined by locked rotor tests and calculated from the equivalent circuit model shown by figure 2.6 using (2.28) giving the results presented in figure 5.2 which shows the effect that different stator currents and frequencies have on the leakage inductance. The current are swept between 25A and 250A while the frequency is swept between 12.5Hz to 1000Hz.

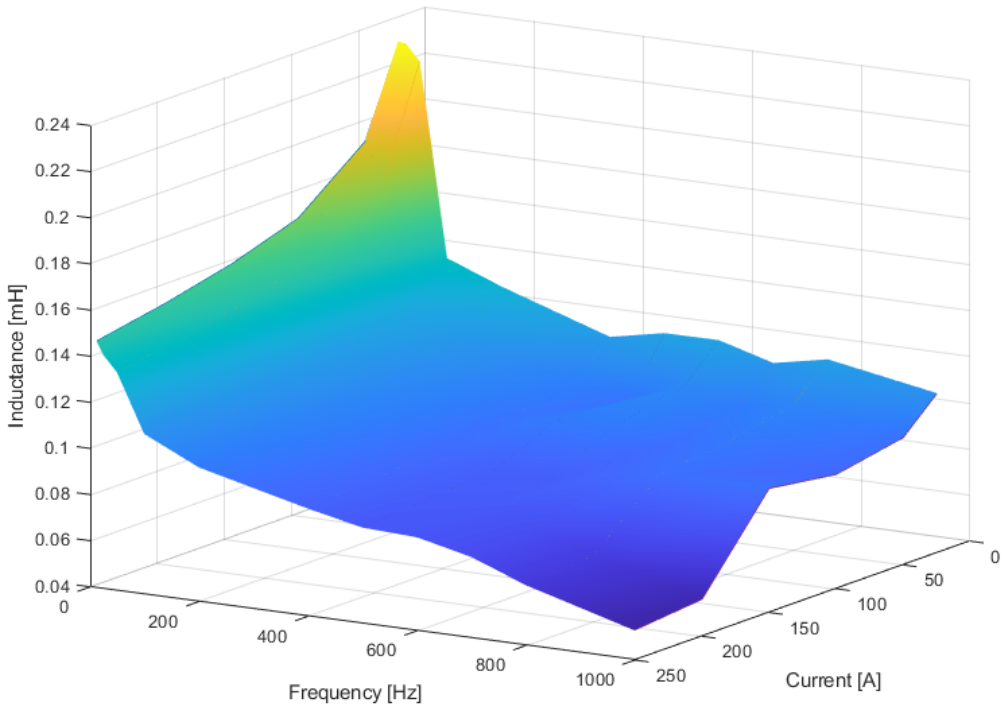

Figure 5.2: Leakage inductance L_σ
for different stator frequencies and current amplitudes.

It can be seen in figure 5.2 that the leakage inductance do not change a lot with substantial changes in current and frequency except for operations at lower frequencies and especially at low frequencies and low current. But the leakage inductance decreases a little as the current and frequency increases.

5.1.2 Magnetising Inductance

The magnetising inductance was determined from different no load tests as explained in section 2.5.4 for different current amplitudes and stator frequencies. The current are swept between 25A and 250A while the frequency is swept between 12.5Hz to 1000Hz.

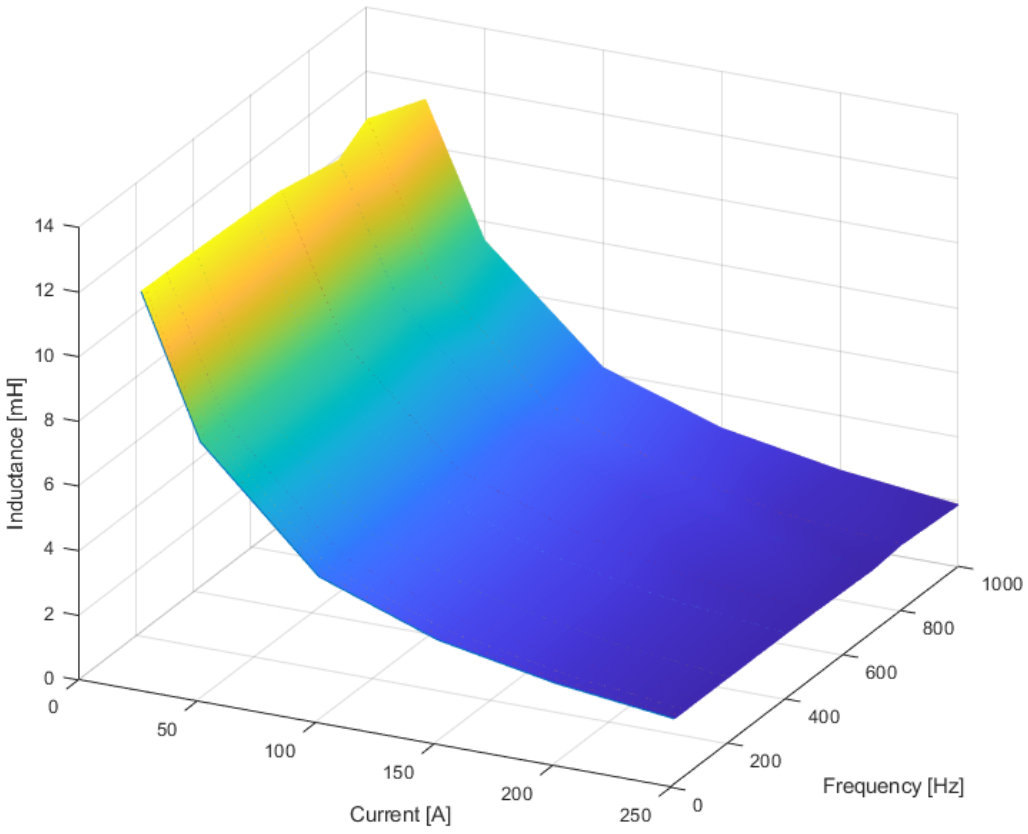

Figure 5.3: Mangetising inductance depending on stator current amplitude and frequency.

It can be seen in the picture that the magnetising inductance mostly depends on the current amplitude that the machine is being supplied with and less of the frequency of that current as the magnetising inductance stay around the same value for the same current amplitude and only increase slightly as the frequency increases.

5.1.3 Core loss resistance

The core loss resistance is the estimated resistance of the core resulting in losses assumed to be resistive and modelled for the stator. The current are swept between 25A and 250A while the frequency is swept between 12.5Hz to 1000Hz.

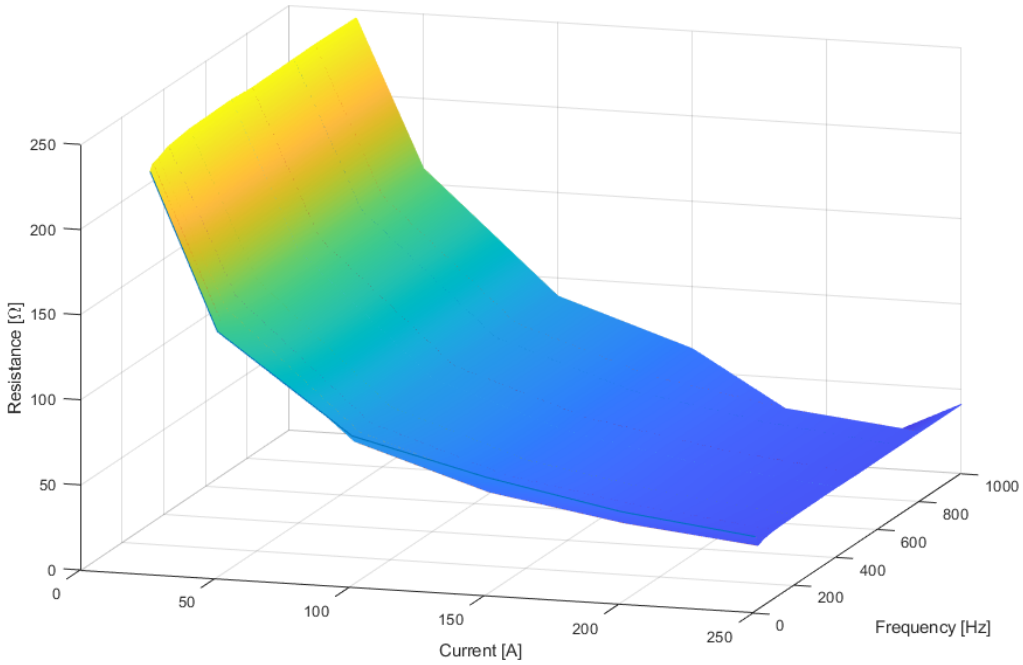

Figure 5.4: Equivalent core resistance dependent on stator current and frequency

It can be seen that the core resistance mostly depends on the current amplitude and not as much on the frequency. This can maybe due that it is modeled as a equivalent ideal lumped resistance that should not depend on frequency.

5.1.4 Minimizing loss control and MTPA

The minimum loss control was implemented as explained in section 2.6.4. Using MATLABs *fmincon* fucntion. The control is meant to minimise the total loss of the machine and this is achieved by selecting the stator dq-currents as well as the frequency, resulting in as low loss as possible while being below maximum current and frequency. In addition to this, the dq-currents should also result in the given operating points in terms of speed and torque. The torque for the operating points are swept from zero to the maximum torque given the specific speed, according to (2.39) and (2.40) until the machine enters the field weakening region, then the torque is given by the dq-currents according to (2.42) and (2.43). The losses for both the controllers are estimated using the power loss of the dq-components (2.51).

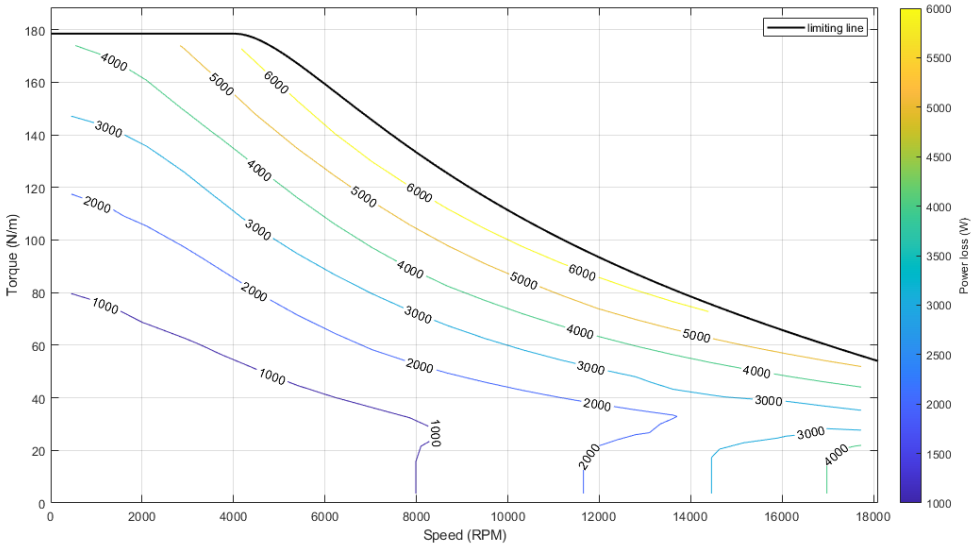

Figure 5.5: Losses from the minimum loss controller for a range of operating points of torque and speed

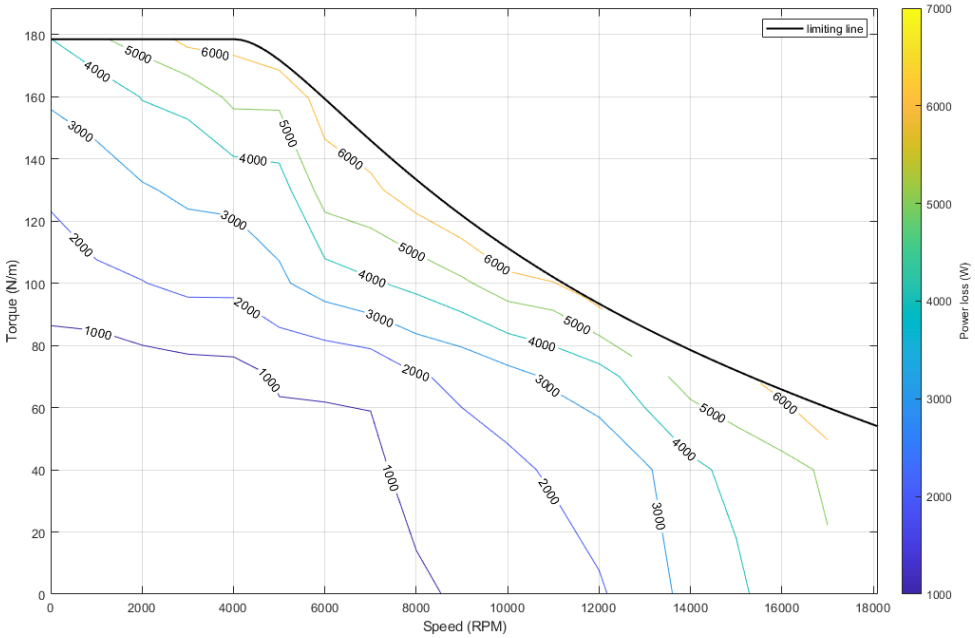

Figure 5.6: Losses from a MTPA controller for a range of operating points

It should be noted that the MTPA losses are calculated with lower number of operating points but the general characteristic of the losses can still be evaluated. Upon comparing the two it can be seen that there is not much difference in loss between them for operation of high torque and lower speeds but that the difference becomes slightly more significant at higher speeds and lower torque. But then the losses are around the same values for that

region as well. It could be beneficial in this case to use the minimum loss controller if the operating point that do result in lower loss is a common operating points for the machine.

5.2 Radial and Tangential Flux Densities on Stator Teeth

Concerning tooth force calculation, only one operating point was observed at 133 Volts rms at 50Hz with 0.61 radians phase angle and this voltage was also used as the reference to generate the the PWM pulses. This type of simulation sequence has already been explained in section 3.6. The forces acting on the tooth of the stator winding was studied at different parts of the tooth which is explained in the next section. At first, the radial and tangential flux densities at the different polyline positions were studied and the plots are shown below.

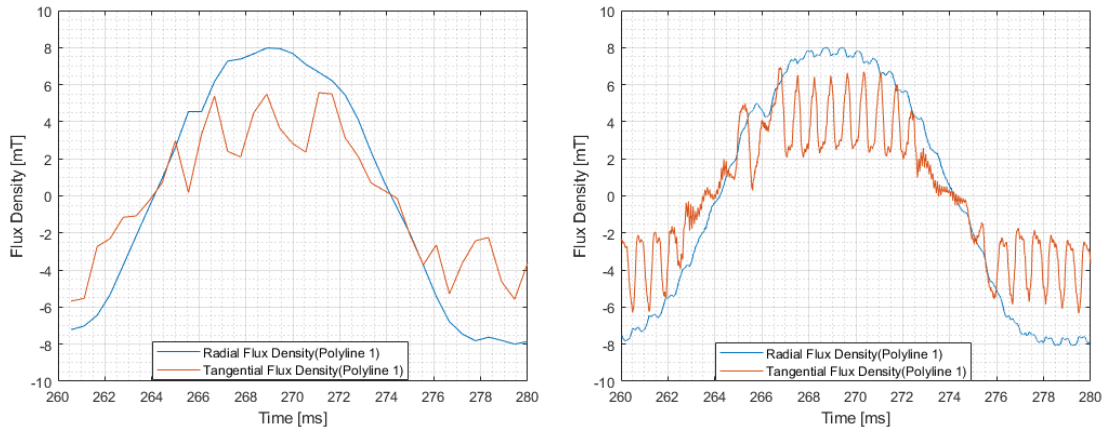

(a) Flux densities with sinusoidal feeding **(b)** Flux densities with PWM feeding

Figure 5.7: Radial and tangential flux density at polyline 1 with sinusoidal and PWM feeding

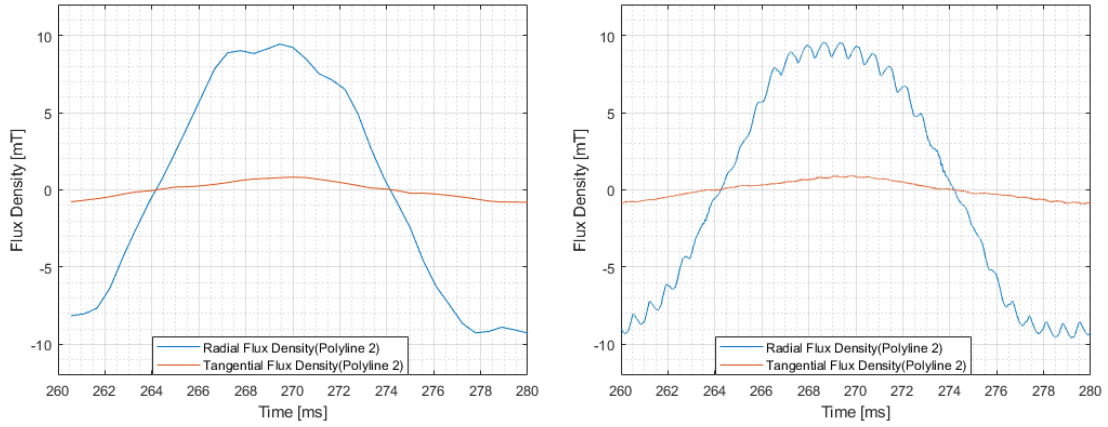

(a) Flux densities with sinusoidal feeding **(b)** Flux densities with PWM feeding

Figure 5.8: Radial and tangential flux density at polyline 2 with sinusoidal and PWM feeding

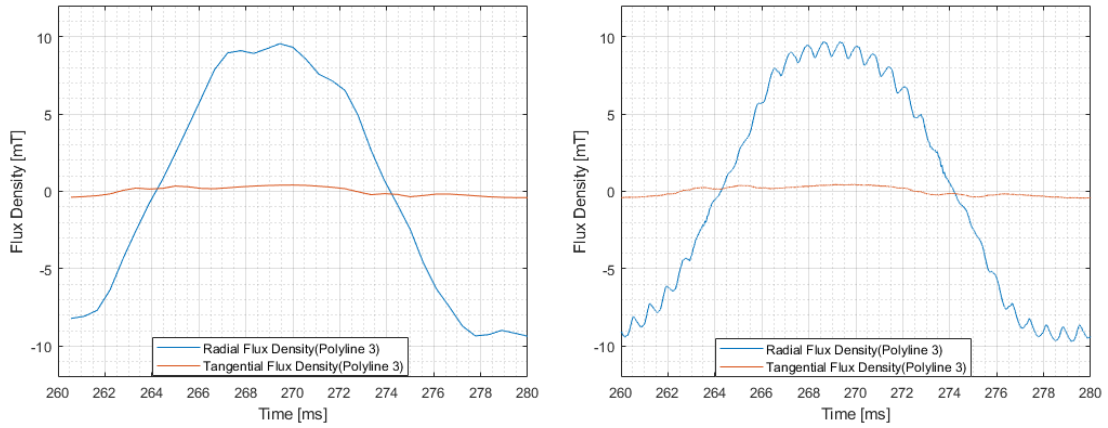

(a) Flux densities with sinusoidal feeding **(b)** Flux densities with PWM feeding

Figure 5.9: Radial and tangential flux density at polyline 3 with sinusoidal and PWM feeding

The radial flux densities along the stator teeth i.e at polyline 1, polyline 2 and polyline 3 are relatively constant. Radial flux as the name suggests flows radially within the stator teeth. The consistent value of radial flux density along the stator teeth is by design as stator windings are usually distributed evenly around the stator core, resulting in a symmetrical arrangement.

However, we can observe that the tangential flux density is highest at the tip of the stator teeth i.e at polyline 1 and decreases as we move away from the stator teeth tips towards the yoke. Magnetic leakage and fringing effect could be possible reasons for this variation in tangential flux density.

Similar radial and tangential flux density behaviour can be observed in PWM feeding but with much higher harmonics, which is expected due to the higher harmonics in the stator current.

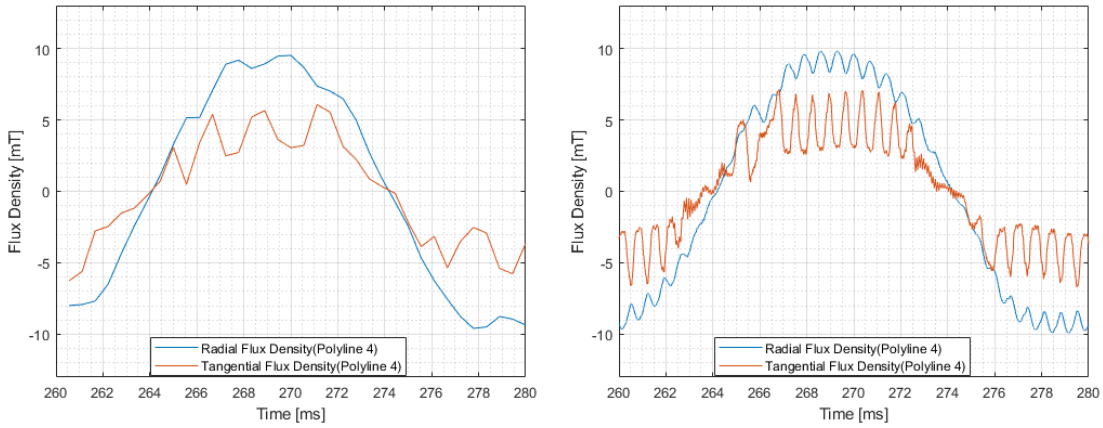

(a) Flux densities with sinusoidal feeding **(b)** Flux densities with PWM feeding

Figure 5.10: Radial and tangential flux density at polyline 4 with sinusoidal and PWM feeding

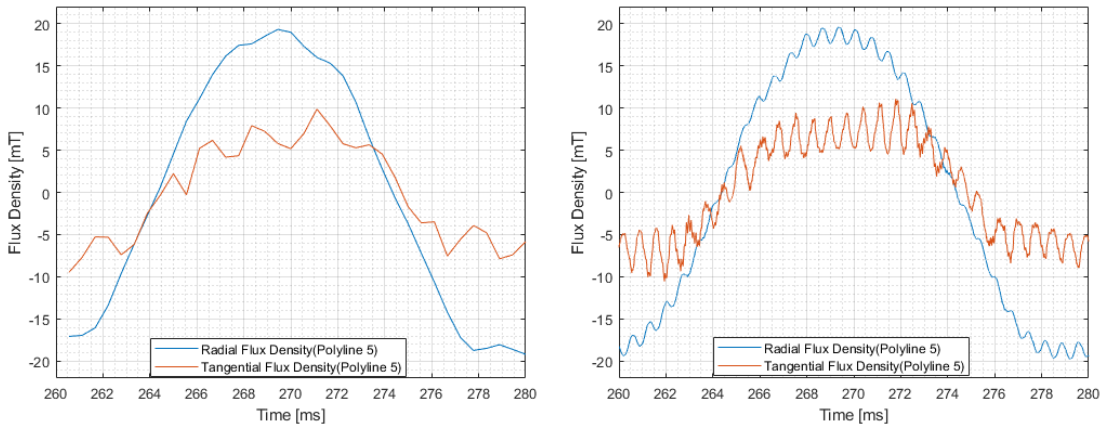

(a) Flux densities with sinusoidal feeding **(b)** Flux densities with PWM feeding

Figure 5.11: Radial and tangential flux density at polyline 5 with sinusoidal and PWM feeding

The leakage flux in the induction motor can be studied by analyzing the magnetic flux density in different regions of the motor. In our case, we can compare the magnetic flux density along polyline 1 and polyline 4 as shown in figures 5.8 and 5.10 .Upon comparison, it is evident that the magnetic flux density at polyline 4 is higher than that at polyline 1. This observation provides valuable insights into the presence of leakage flux in the motor. Polyline 1 extends over only one stator tooth, while polyline 4 spans from the middle of one slot to the middle of another slot. This difference in the extent of coverage explains the variation in magnetic flux density.

The higher magnetic flux density along polyline 4 indicates a larger amount of flux leakage between adjacent stator teeth and slots. In contrast, along polyline 1, the flux is confined within a single stator tooth, resulting in a lower magnetic flux density due to a

more constrained flux path.

Polyline 5 extends over the middle of one slot to the middle of another but it spans over two stator tooth. The flux density of polyline 5 line is shown in figure 5.11 which is almost twice the flux density as that of polyline 4. It is expected that the flux density along polyline 5, which spans over two stator teeth, would be higher compared to the flux density along polyline 4, which covers almost half of the length of polyline 5.

The use of such lines to study fluxes helps in understanding and quantifying the leakage flux in an induction motor. This knowledge is crucial for motor designers to optimize the motor design, minimize flux leakage, and improve motor efficiency and performance.

5.3 Radial and Tangential Force on Stator Teeth

In the previous section we looked at the fluxes at the different parts of the tooth. In this section, we will look into the forces acting on the different parts of the tooth due to the interaction of those fluxes. As we already have the information about the radial and tangential fluxes, it is easy to calculate the radial and tangential forces acting on those parts with the help of the Maxwell Stress Tensor Equation which is explained in section 2.1. Due to the computational time limit, it was only possible to obtain data for one electrical cycle of 20ms. The radial and tangential forces acting on the tooth while the machine is being excited by both purely sinusoidal and PWM feeding are shown in figure 5.12.

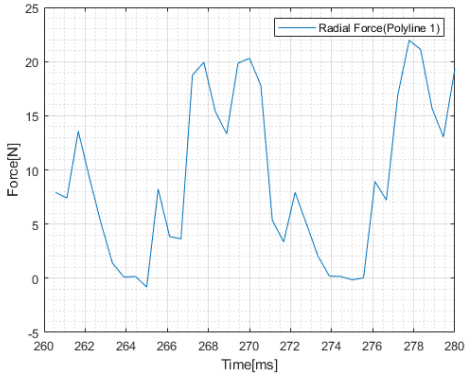

(a) Radial force with sinusoidal feeding

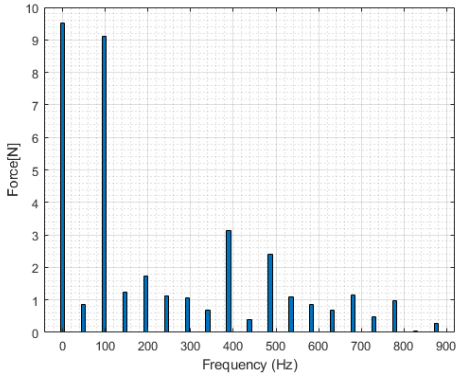

(b) FFT

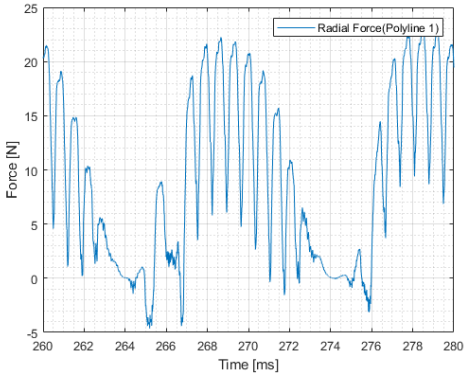

(c) Radial force with PWM feeding

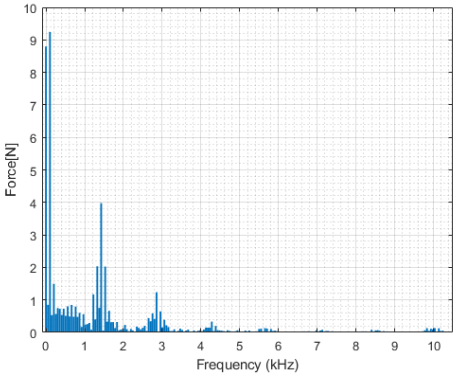

(d) FFT

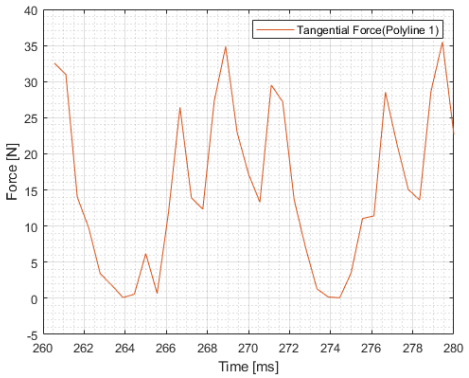

(e) Tangential force with sinusoidal feeding

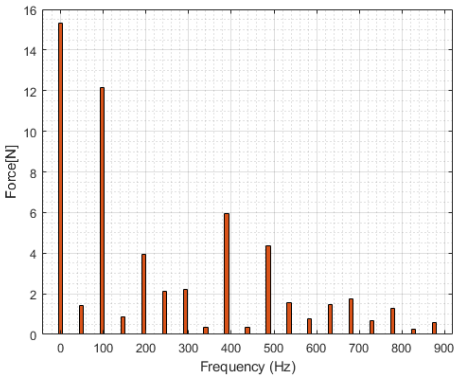

(f) FFT

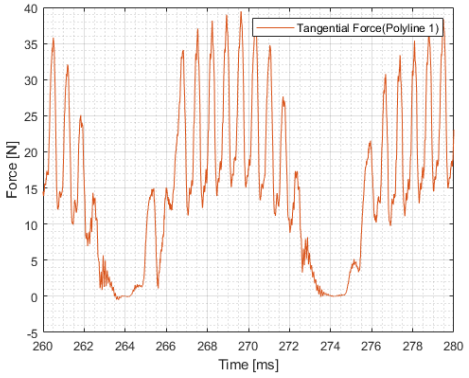

(g) Tangential force with PWM feeding

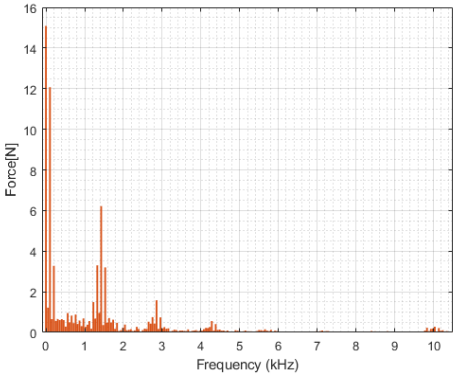

(h) FFT

Figure 5.12: Forces acting on polyline 1 with sinusoidal and PWM feeding with corresponding FFT

Looking at the the forces and FFT plots for sinusoidal feeding in the figures, we can see that we have two peaks that stand out at 0 Hz and at 100 Hz with sinusoidal feeding but not present at PWM feeding. The peaks at this frequency can be explained with the equations used to calculate the tooth forces.

We estimated the forces using Maxwell Stress Tensor equations (2.1) and (2.2) where we multiply the radial and tangential flux density. The result of multiplying these two waveforms gives a composite waveform which has very different characteristics compared to the originals. The two new dominant harmonics can be observed in the tooth forces at the sum and difference of the original signals frequencies.

$$sin(2\pi f_1 t)sin(2\pi f_2 t) = \frac{1}{2}cos[2\pi(f_1 - f_2)t] - \frac{1}{2}cos[2\pi(f_1 + f_2)t] \tag{5.1}$$

As the two signals in this case both are of $50Hz$ fundamental frequency the difference become zero and the sum becomes $100Hz$.

In the FFT analysis of the radial and tangential tooth forces with sinusoiudal feeding, it is possible to observe additional harmonic components apart from the fundamental frequency and second harmonics. However, it is important to note that these harmonics generally exhibit significantly lower magnitudes, with one notable exception. The 8^{th} order harmonics, occurring at a frequency of 400Hz, demonstrate a more substantial magnitude.It is worth mentioning that when examining frequencies above 900Hz for sinusoidal feeding, the magnitudes of the harmonics are consistently below 2 Nm. This finding suggests that the influence of these higher-frequency harmonics on the overall tooth forces is relatively small.

Similarly, analysing the tooth forces with PWM feeding, a series of harmonics components can be observed other than at 0Hz and 100Hz, whose presence has been explained before. Interestingly, as the frequency of these harmonics increases, they naturally become suppressed. This is a result of the inherent characteristics of PWM, which tend to reduce the amplitudes of higher-frequency harmonics.

However, a notable observation can be made in the waveforms of radial and tangential forces when utilizing pulse width modulation (PWM) feeding. These waveforms exhibit slight periodic fluctuations and looking at corresponding FFT we can see a peak at around frequency of 1420 Hz. This interesting phenomenon is further discussed in the sub section 5.3.1

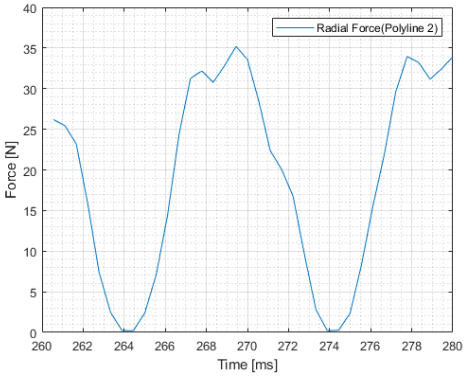

(a) Radial force with sinusoidal feeding

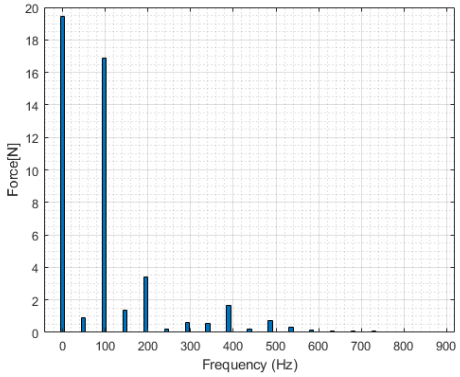

(b) FFT

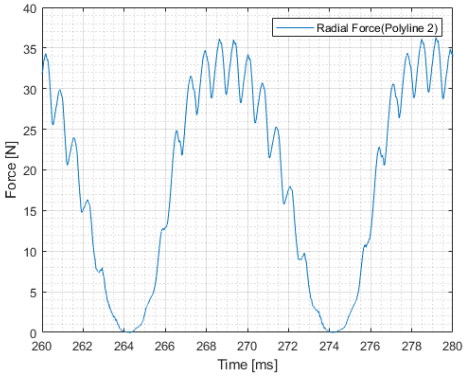

(c) Radial force with PWM feeding

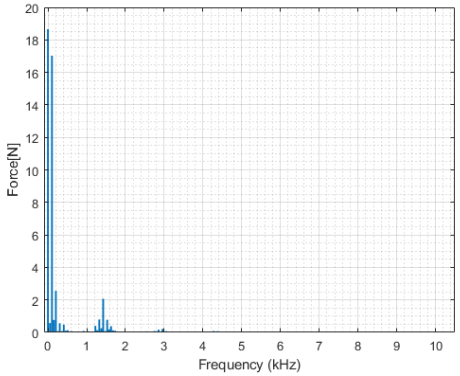

(d) FFT

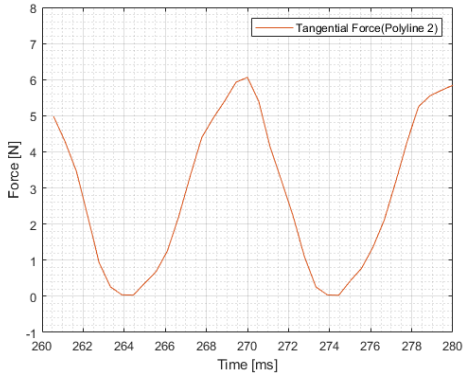

(e) Tangential force with sinusoidal feeding

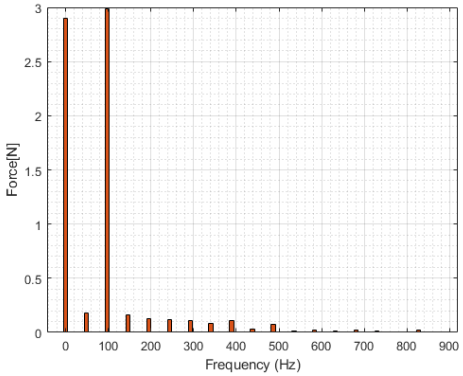

(f) FFT

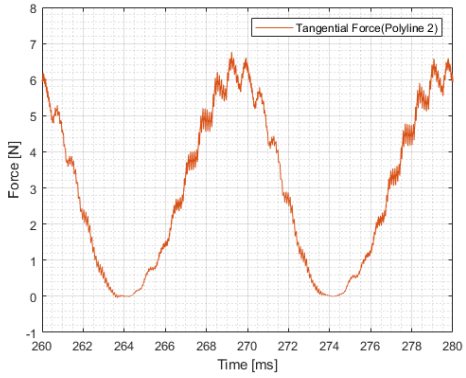

(g) Tangential force with PWM feeding

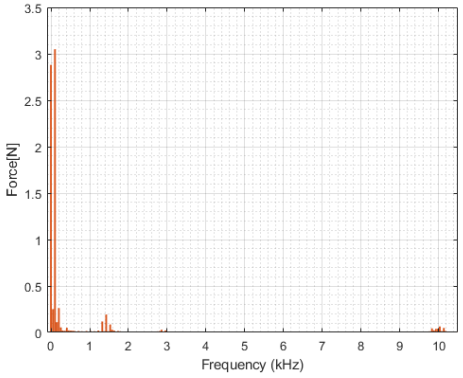

(h) FFT

Figure 5.13: Forces acting on polyline 2 with sinusoidal and PWM feeding with corresponding FFT

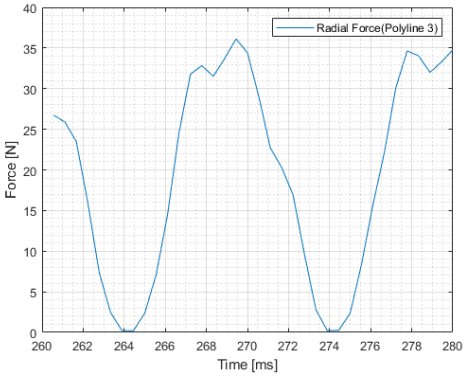

(a) Radial force with sinusoidal feeding

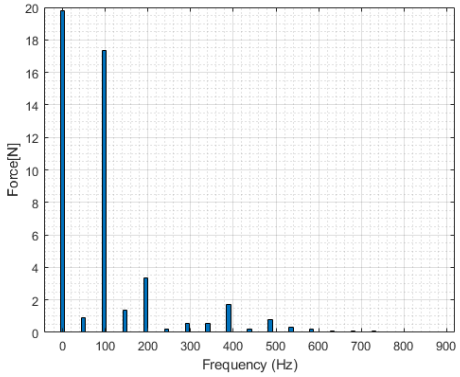

(b) FFT

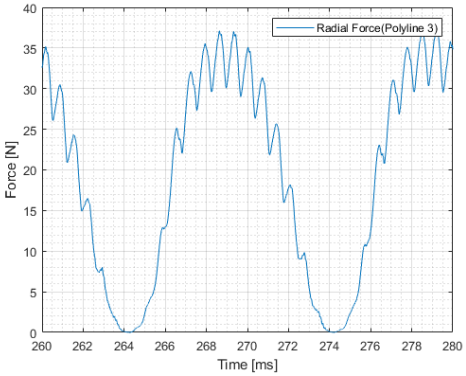

(c) Radial force with PWM feeding

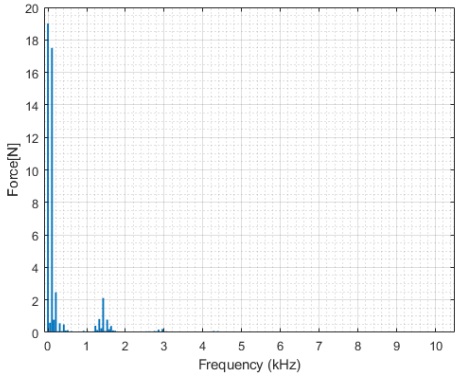

(d) FFT

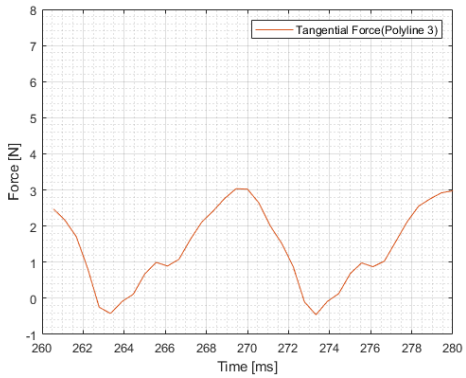

(e) Tangential force with sinusoidal feeding

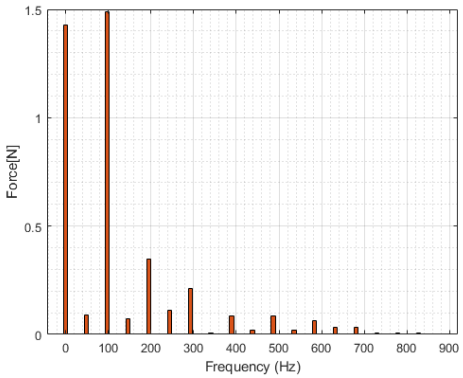

(f) FFT

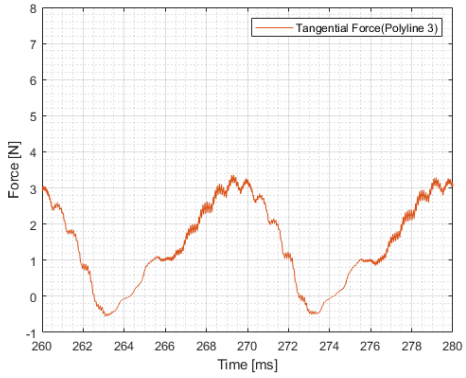

(g) Tangential force with PWM feeding

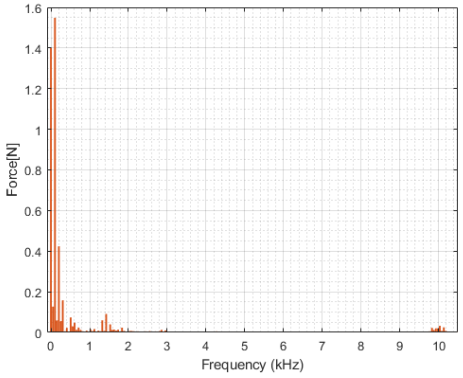

(h) FFT

Figure 5.14: Forces acting on polyline 3 with sinusoidal and PWM feeding with corresponding FFT

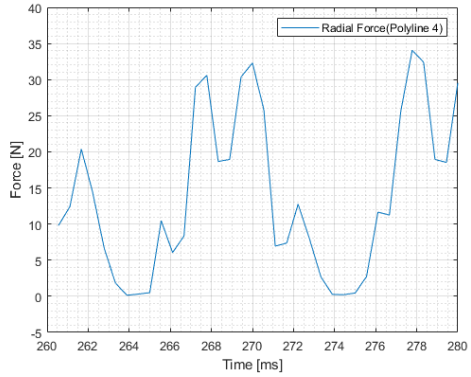

(a) Radial force with sinusoidal feeding

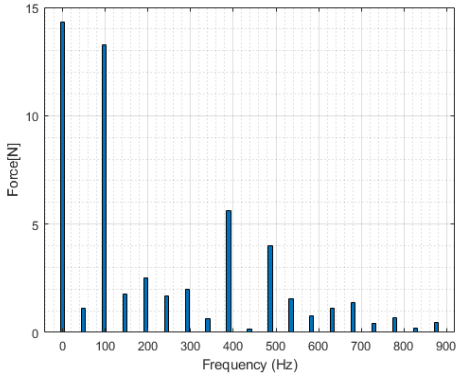

(b) FFT

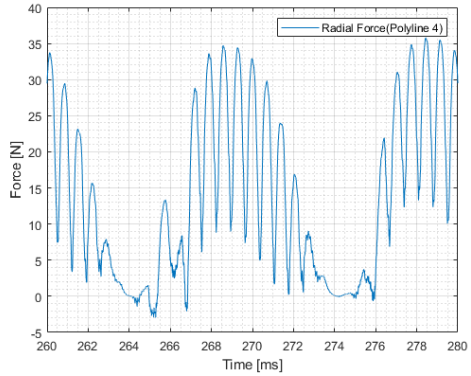

(c) Radial force with PWM feeding

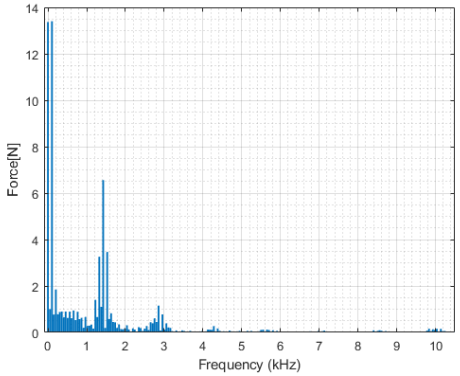

(d) FFT

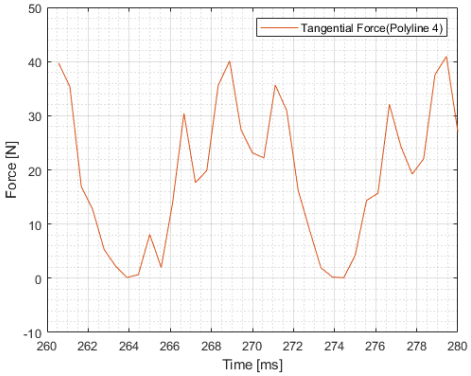

(e) Tangential force with sinusoidal feeding

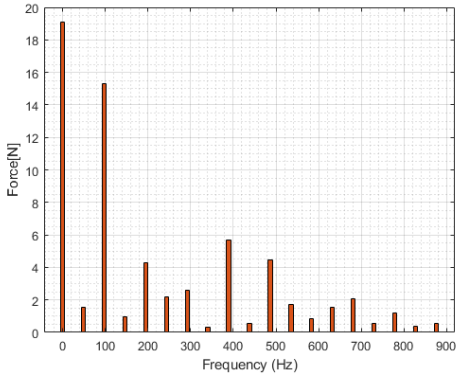

(f) FFT

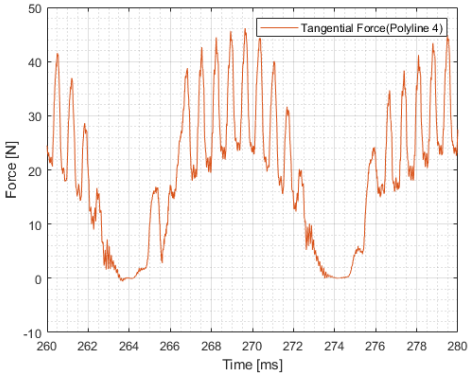

(g) Tangential force with PWM feeding

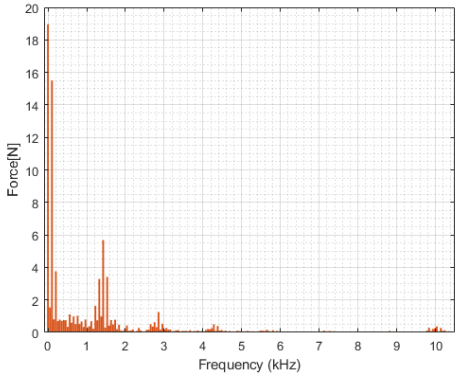

(h) FFT

Figure 5.15: Forces acting on polyline 4 with sinusoidal and PWM feeding with corresponding FFT

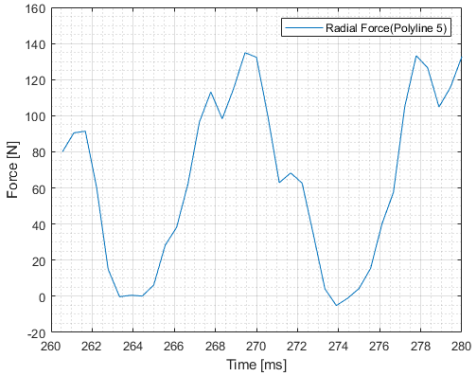

(a) Radial force with sinusoidal feeding

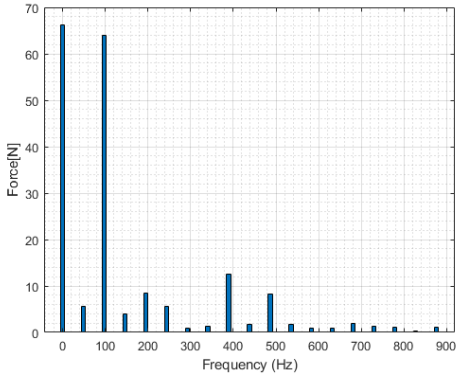

(b) FFT

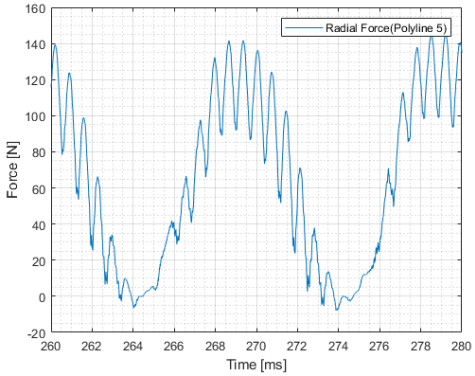

(c) Radial force with PWM feeding

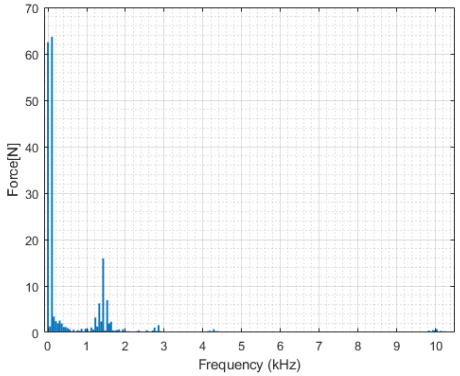

(d) FFT

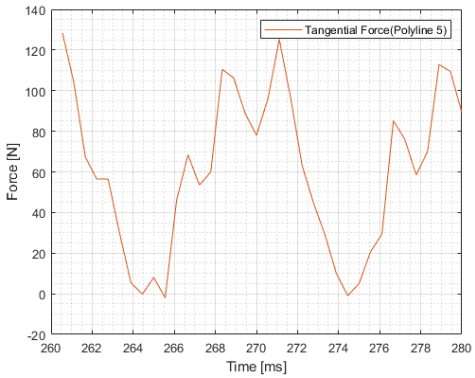

(e) Tangential force with sinusoidal feeding

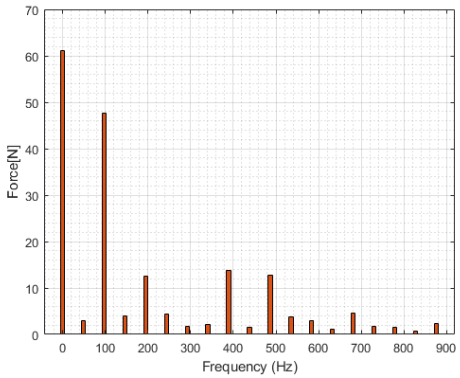

(f) FFT

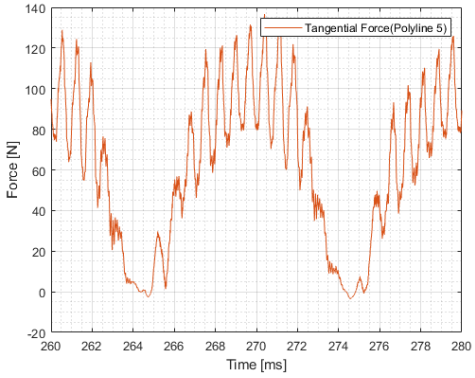

(g) Tangential force with PWM feeding

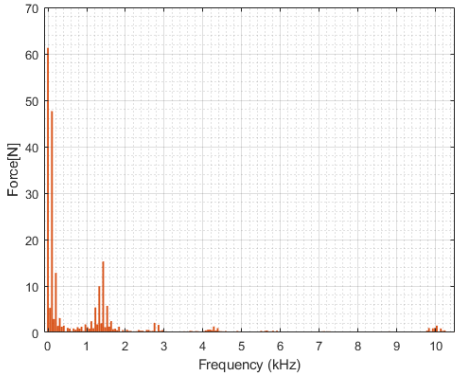

(h) FFT

Figure 5.16: Forces acting on polyline 5 with sinusoidal and PWM feeding with corresponding FFT

5.3.1 Influence of rotor bar motion and current on force oscillation

One thing that could affect the oscillation and ripple of the radial and tangential forces could be the influence of rotor bars passing over a teeth affecting the field and flux of the stator teeth. To investigate if this is causing any oscillation, the frequency of the rotor bars rotation are compared with the corresponding frequencies and amplitude who make up the force wave forms given from FFT. Where the frequency of the rotor bar movement is given by

$$f_{bars}[Hz] = \frac{\omega_r[rpm]}{60} Q_r \tag{5.2}$$

where Q_r is the number of rotor bars.

To clarefy the f_{bars} frequency is the frequency of rotor bars passing over a stator teeth. Meaning that if one rotor bar is aligned with the center of a stator teeth this frequency is the rate of which it take for the next rotor bar to be aligned with the same stator teeth.

In the cases above $50Hz$ stator frequency and a slip equal to 0.02, the rotor speed is $1470rpm$ and the resulting frequency of the bars movement is around $1421Hz$. This is very close to the frequency of one of the higher peak in the FFT amplitude-frequency figure generated from the simulation results with PWM feeding with 50Hz reference and a $10kHz$ carrier wave. As can be seen as a prominent part of the FFT analysis of figures 5.12d and 5.12h. These harmonics content appears in both the radial and tangential teeth forces and greatly influence the oscillation of the teeth forces during one period as it at this frequency is several orders of magnitudes higher than the fundamental, in this case of 50Hz.

5.4 Torque Ripple

The torque waveforms for one electrical cycle in steady state is shown in figure 5.17 where 133 volts rms purely sinusoidal voltage was applied as input voltage for the sinusoidal feeding and this voltage was used as a reference to generate the PWM signals. With purely sinusoidal voltage feeding, an average torque of 260 Nm with ripple around 3.25% was obtained at 1470 rpm and 2% slip, which can be observed from figures 5.17a and 5.18a.

A reduced torque of average value 250 Nm was obtained at 1470 rpm and 2% slip with PWM feeding. As explained in the previous section, when PWM is used, the voltage waveform applied to the motor windings consists of discrete pulses with varying widths. These voltage pulses give rise to higher current ripple which ultimately results in higher torque ripples. A torque ripple around 14.6% can be observed with PWM feeding which can be seen in figure 5.17b.

Table 5.1: Comparison of torque with sinusoidal and PWM feeding at 133 volts

Description	Sinusoidal feeding	PWM feeding
Average Torque	260 Nm	250 Nm
Ripple	3.25%	14.5 %

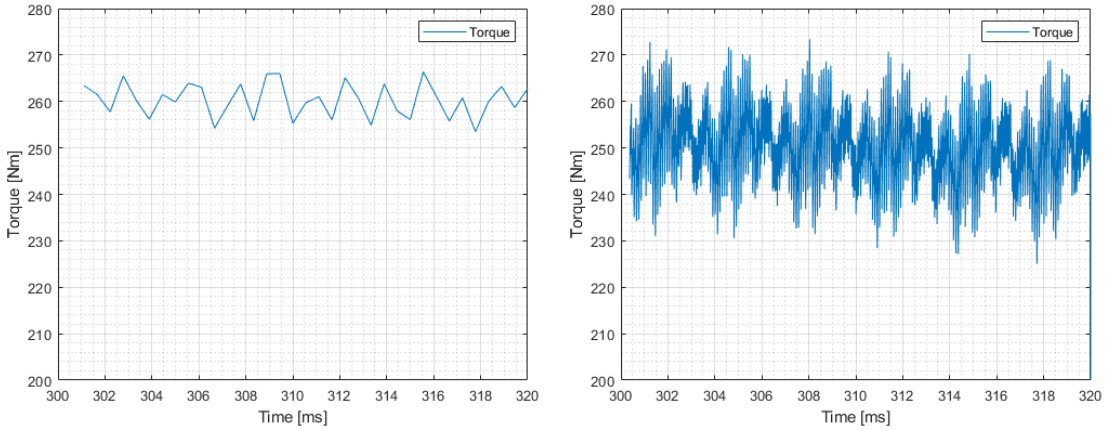

(a) Torque with sinusoidal feeding **(b)** Torque with PWM feeding

Figure 5.17: Comparison of the torque obtained with sinusoidal and PWM feeding at 133 Volts

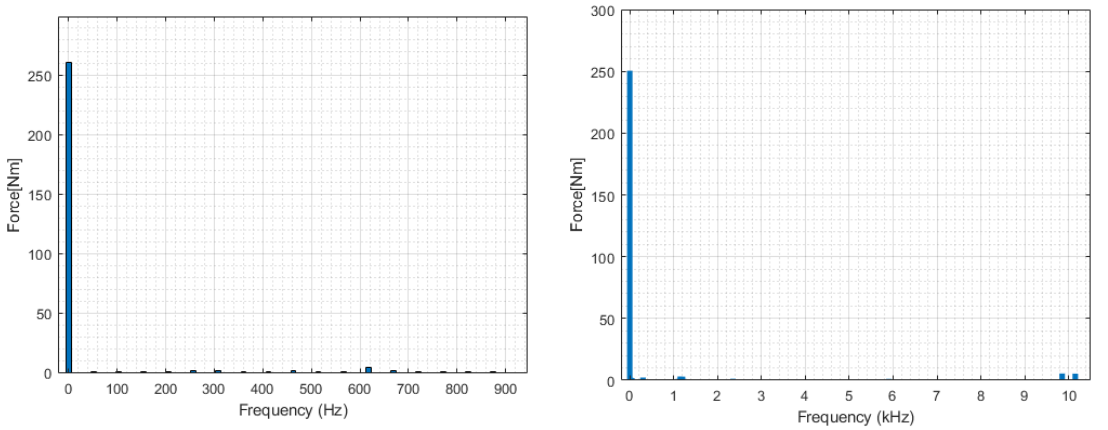

(a) Torque with sinusoidal feeding **(b)** Torque with PWM feeding

Figure 5.18: FFT of the torque obtained with sinusoidal and PWM feeding at 133 volts

When evaluating the frequency decomposition of the torque with PWM feeding, it can be seen in figure 5.18b that the FFT coefficients associated with torque ripple are consistently below 5 Nm for frequencies other than 0 Hz . Additionally, these coefficients are further suppressed beyond 10 kHz, which corresponds to the PWM switching frequency. As the mechanical system has higher inertia, these torque harmonics will not propagate to the drivetrain.

The difference in the average torque obtained with two different excitation strategy can be attributed to the the harmonics, losses and reduced input excitation with the PWM feeding. Due to the discrete nature of voltage impulses from PWM, torque ripples are introduced resulting in variations in torque output as observed in figure 5.17b. Such a variation in the torque output leads to a lower average torque compared to the sinusoidal voltage feeding case, which typically provides a smoother torque output. Another prospective to consider can be the current harmonics in the motor current by PWM feeding which increase losses in the motor. These losses can contribute to a decrease in the average torque compared to the sinusoidal voltage feeding, which typically has lower harmonic content.

The effect of PWM feeding on torque ripple was also studied with stator excitation of 140.8 volts. With purely sinusoidal voltage feeding, an average torque of 297.985 Nm with ripple around 3.35% was obtained and with PWM feeding an average torque of 292 Nm with ripple around 14% which can be seen in figures 5.19 and 5.20. It can be observed that the torque ripple did not increase significantly with increase in excitation.

Table 5.2: Comparison of torque with sinusoidal and PWM feeding at 140.8 volts

Description	Sinusoidal feeding	PWM feeding
Average Torque	298 Nm	292 Nm
Ripple	3.35%	14 %

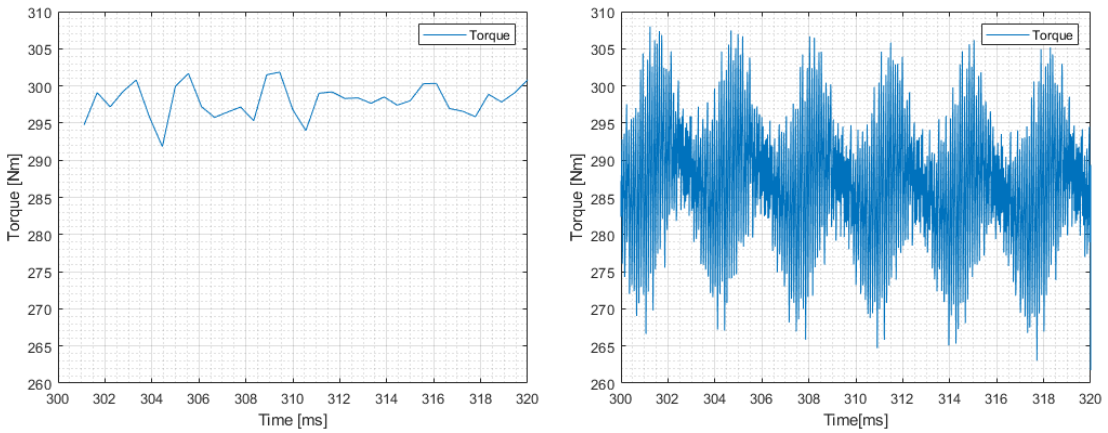

(a) Torque with sinusoidal feeding **(b)** Torque with PWM feeding

Figure 5.19: Comparison of the torque obtained with sinusoidal and PWM feeding at 140.8 Volts

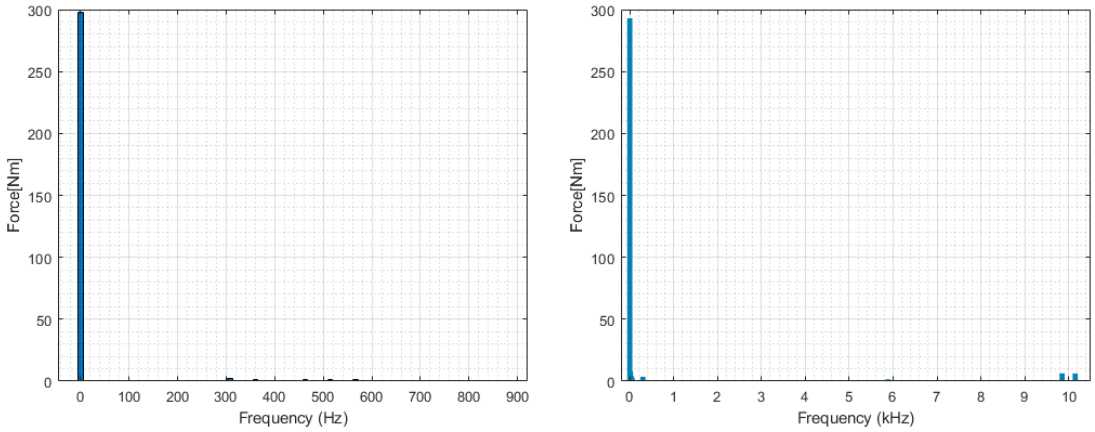

(a) Torque with sinusoidal feeding **(b)** Torque with PWM feeding

Figure 5.20: FFT of the torque obtained with sinusoidal and PWM feeding at 140.8 volts

5.5 Losses

A similar approach as the torque ripple studies was taken for the study of losses and efficiency. At first the losses and efficiency with purely sinusoidal voltage of $133 V rms$ and the pwm pulses generated with this sinusoidal voltage as reference was studied. The plots for the different types of losses are shown in figure 5.21 and the summarized information can be found in table 5.3. As we can see from the table, there is significant increase in the eddy current loss and hysteresis loss when the excition was changed from purely sinusoidal voltage excitation to PWM excitation. The average eddy current loss was found to be around 12.42 watts with sinusoidal voltage excitation which almost increased by 5 times to 58.52 watts with pwm feeding. The hysteresis loss increased by 11.41% when the IM was excited with PWM as compared to sinusoidal voltage. So, in overall the coreloss increased by 46.22%. This is in contrast to copper loss where it increased from an average value of 3.31 kilowatts with purely sinusoidal voltage feeding to 3.40 kilowatts with PWM feeding which corresponds to just a 3% increase.

Table 5.3: Comparison of losses with sinusoidal and PWM feeding at voltage magnitude of 133 volts

loss	Sinusoidal Feeding	PWM Feeding
Eddy Current Loss	12.42 w	58.52 w
Hysteresis Loss	115.95 w	129.18 w
Core Loss	128.37 w	187.71 w
Copper Loss	3.31 kw	3.41kw
Total Loss	3.43 kw	3.59 kw
Efficiency	93.62 %	93.33 %

Eddy current loss occurs usually due to the circulating currents induced in the conducting parts of the machine, such as stator core and rotor. These circulating currents leads to resistive losses and dissipate the energy in the form of heat. The rapidly switched voltage

pulses in pwm creates high-frequency harmonics in the machine's magnetic field, which in turn induce additional eddy currents in the conducting parts, thus increasing eddy current losses and this can be realized with the simulation results presented in tables 5.3 and 5.4.

Hysteresis loss is caused by the repeated magnetization and demagnetization of the magnetic materials, primarily the rotor and stator cores. This loss occurs due to the energy required to align and realign the magnetic domains in these materials as the magnetic field changes. PWM feeding can contribute to hysteresis loss by introducing rapid changes in the magnetic field, leading to more frequent magnetization and demagnetization cycles. These rapid transitions result in a increased energy dissipation and a higher hysteresis losses.

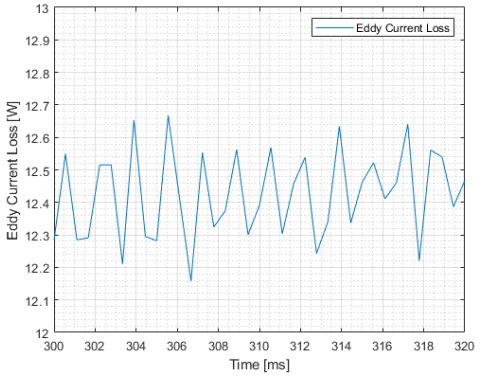

(a) Eddy current loss with sinusoidal

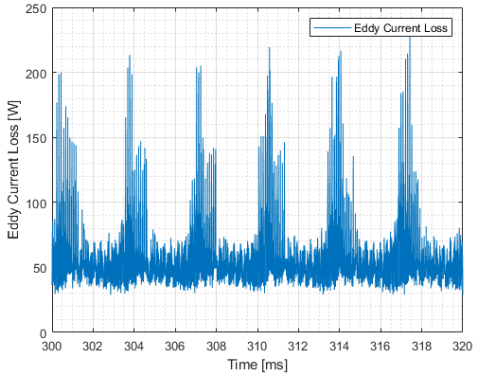

(b) Eddy current loss with PWM feeding

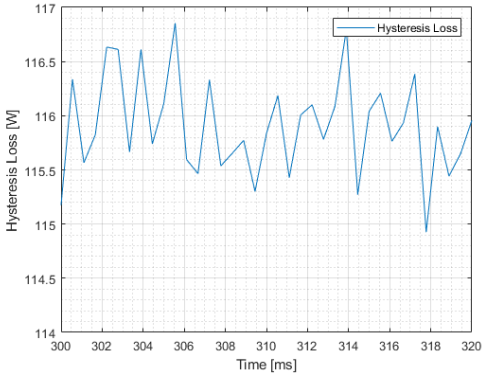

(c) Hysteresis loss with sine feeding

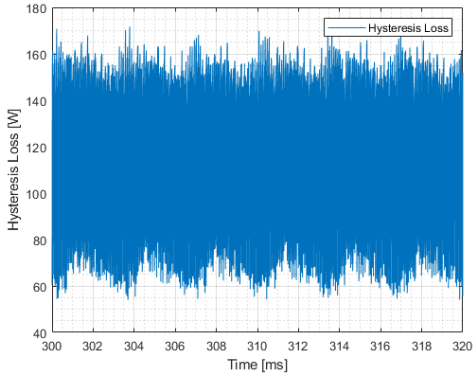

(d) Hysteresis loss with PWM feeding

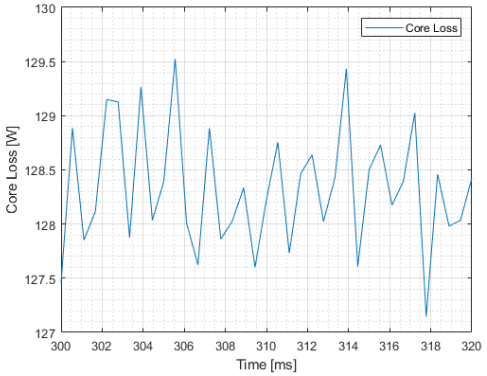

(e) Core loss with sine feeding

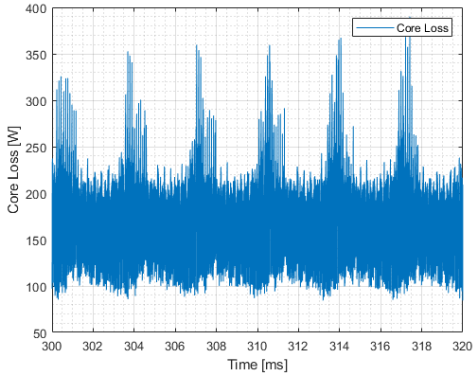

(f) Core loss with PWM feeding

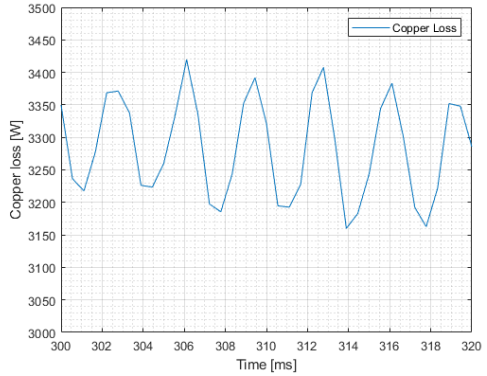

(g) Copper loss with sine feeding

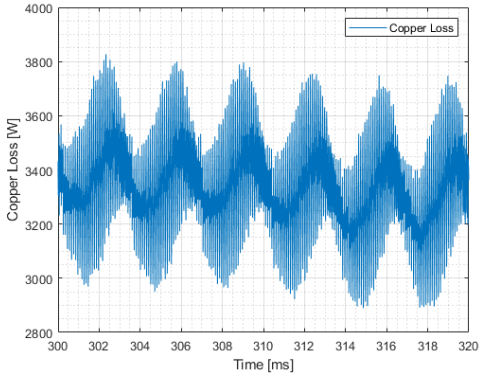

(h) Copper loss with PWM feeding

Figure 5.21: Different losses with sinusoidal and PWM feeding at 133 volts

The increase in copper losses can be attributed to the harmonic contents in current. The PWM waveforms consist of multiple switching frequencies that create higher-frequency harmonics in the machine's current waveform. The presence of harmonics in the current waveform also results in skin effect and proximity effect in the windings. The skin effect causes the current to concentrate near the surface of the conductor, which causes an effective increase in resistance. The proximity effect leads to non-uniform current distribution within the windings, further increasing the resistive losses. The harmonics in the current also induce additional circulating currents in the windings resulting in increased copper losses.

Table 5.4: Comparison of losses with sinusoidal and PWM feeding at voltage magnitude of 140.8 volts rms

loss	Sinusoidal Feeding	PWM Feeding
Eddy Current Loss	13.8396 w	59.6032 w
Hysteresis Loss	127.3997 w	141.2479 w
Core Loss	141.2393 w	200.8510 w
Copper Loss	4.1476 kw	4.3111 kw
Total Loss	4.2889 kw	4.511 kw
Efficiency	93.65 %	93.32 %

Upon examining the losses for the Induction Machine (IM) when excited with 140.8 volts, it was observed that with sinusoidal feeding, the average eddy current loss amounted to 13.8396 watts, while with PWM feeding, it increased to 59.6032 watts. This represents an almost four-fold increase in eddy current loss. Additionally, a 10% increase in hysteresis loss was observed when transitioning from sinusoidal to PWM excitation. Overall, the core loss exhibited a substantial 42.2% increase, rising from 141.2393 watts to 200.8510 watts with the two afore mentioned excitations. In terms of copper loss, sinusoidal excitation resulted in 4.1475 kilowatts, whereas PWM excitation led to 4.3111 kilowatts, corresponding to a 3.94% increase.

Hence, analysis reveals that PWM feeding leads to a substantial percentage increase in core losses in the induction machine, particularly with regards to eddy current losses, which rose by approximately four to five times for the selected operating points. Hysteresis losses also show a notable increase, although not as significant as eddy current losses. In contrast, the copper losses exhibit the smallest percentage increase, approximately around $3-4\%$. Thus, while PWM excitation does result in a modest rise in copper losses, its impact on core losses, especially eddy current losses, is significantly more pronounced.

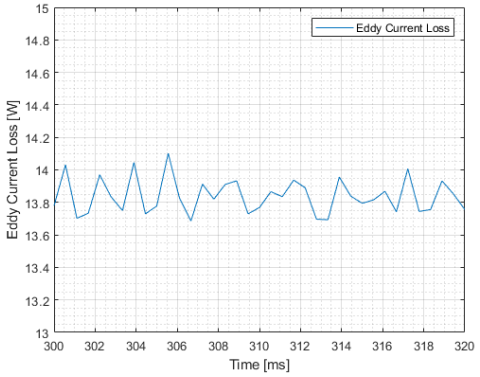

(a) Eddy current loss with sinusoidal

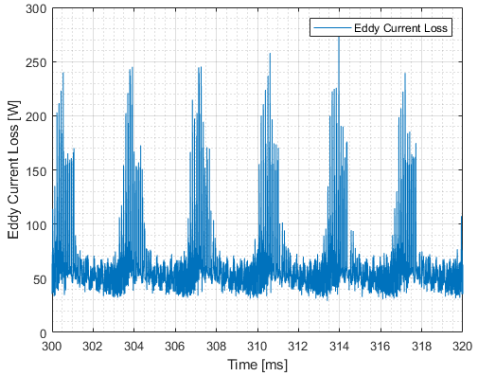

(b) Eddy current loss with PWM feeding

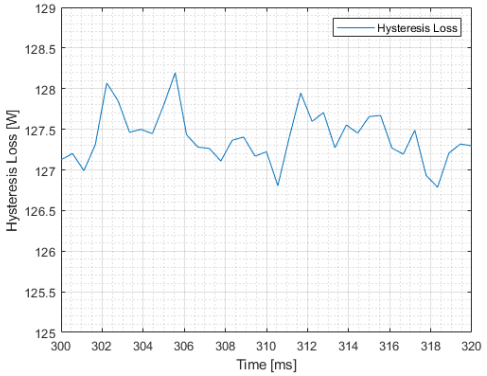

(c) Hysteresis loss with sine feeding

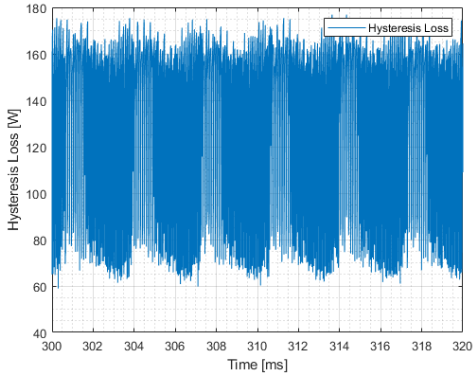

(d) Hysteresis loss with PWM feeding

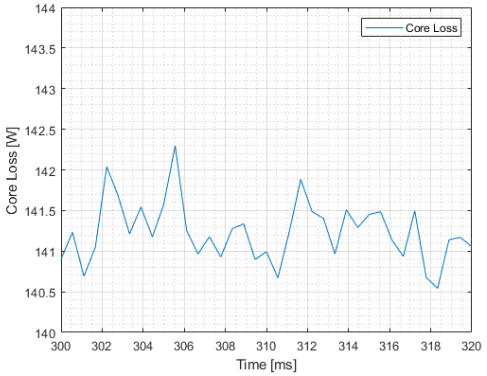

(e) Core loss with sine feeding

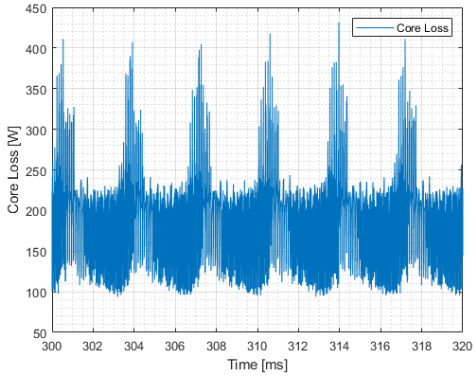

(f) Core loss with PWM feeding

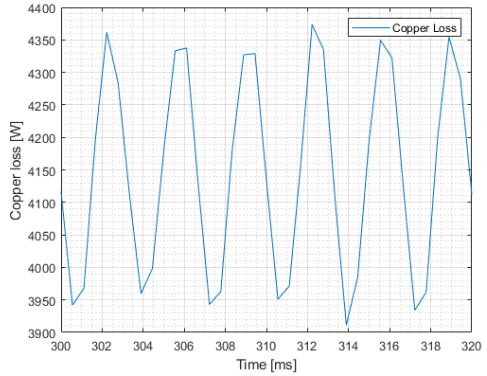

(g) Copper loss with sine feeding

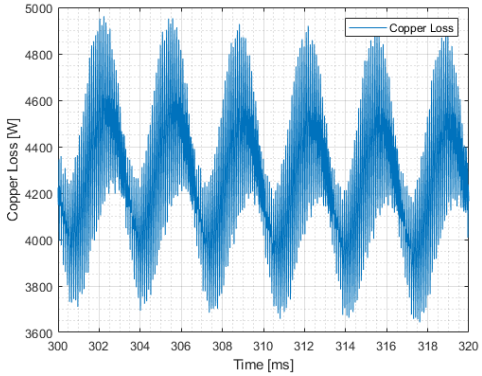

(h) Copper loss with PWM feeding

Figure 5.22: Different losses with sinusoidal and PWM feeding at 140.8 volts

6

Sustainability and Ethical Aspects

6.1 Sustainability Impact

The transportation sector has significant impact on the environment and green house gas emission. Transport accounts for around one-fifth of global carbon dioxide (CO_2) emissions. About three-quarters of transport emissions is accounted by the road travel. Most of these emissions comes from passenger vehicles like cars and buses, contributing around 45% and the remaining 29% comes from trucks carrying freight[10]. Upon focusing our attention specifically on the European Union, transport was responsible for about a quarter of the EU's total CO_2 emissions in 2019, of which 72% came from road transportation. Passenger cars are a major polluter, accounting for 61% of total CO_2 emissions from EU road transport[11]. As most countries have agreed to the Paris agreement goal of green house gas emission only accounting for an rise in average global temperature of $1.5^{\circ}C$[12] the green house gas emissions from transport should be dramatically reduced. One of the ways to reduce the CO_2 emission could be an more extensive use of electrical vehicles running on renewable electricity instead of internal combustion powered vehicles running on fossil fuels. Fortunately, electric cars are gaining traction, representing 18% of all new registered passenger vehicles in 2021 which is a significant increase from 11% in 2020[11].

The use of the induction motors in the EVs could also help in our goal towards sustainability and carbon neutrality. Due to the robustness, load handling, low cost, low maintenance requirement, the induction machine is a convincing choice in EVs. Additionally, the easily reusable and recyclable materials utilized in induction machines as no permanent magnets are needed in the design further contribute to their appeal as environmentally-friendly options for EVs. More research, development and innovation in induction motors can help electrify the global transport sector and make the transition to clean energy faster.

6.2 Ethical Aspects

It is highly appreciative that the world is moving towards EVs from fossil fuel powered vehicles. However, most the EVs employ PMSM and all known strong magnets contain rare earth (RE) elements. Rare earth elements such as Nd and Dy have become critical materials due to the growing demand and constrained supply[13]. It is also important to highlight that these rare earth metals have environmental implications during mining. Furthermore, it is unfortunate that some regions associated with serious human rights violations are involved in the extraction of these materials. This reality highlights the

complex ethical considerations surrounding the supply chain of these critical materials.

By opting for induction motors that do not require the use of permanent magnets, we can effectively decrease the demand for rare earth elements and subsequently contribute to the reduction of environmental pollution caused by their mining. This approach also aligns with our moral obligation to abstain from sourcing materials from regions or countries involved in human rights violations and the possible exploitation of child labor in the extraction of raw materials necessary for PMSM.

Furthermore, as a authors of this thesis and students of electrical engineering, we always have uphold the Code of Ethics outlined by the IEEE organisation throughout our thesis work. As the very first point of IEEE Code of Ethics reads *"to hold paramount the safety, health, and welfare of the public, to strive to comply with ethical design and sustainable development practices, to protect the privacy of others, and to disclose promptly factors that might endanger the public or the environment;"*, we have tried to make sure that our design and modelling choices always take environmental factor into the consideration and promote sustainability.

As the authors, we are committed to upholding the principles outlined in the seventh point of the IEEE Ethics code which states *"to treat all persons fairly and with respect, and to not engage in discrimination based on characteristics such as race, religion, gender, disability, age, national origin, sexual orientation, gender identity, or gender expression;"*. We firmly believe in treating all individuals fairly and with utmost respect, and we are dedicated to ensuring that our work does not condone with any form of discrimination. This commitment shows our dedication to fostering an inclusive environment and promoting a fair and impartial research environment that embraces the diversity of all individuals.

6.3 Societal Impact

Electric vehicles (EVs), in general, have far-reaching societal and environmental implications. First and foremost, EVs contribute to environmental sustainability and help combat air pollution and reduce greenhouse gas emissions. This has a positive effect on air quality, mitigates the effects of climate change, and creates a healthier environment for all.

By employing efficient induction motors help reduce energy consumption. This conservation of energy benefits society by reducing reliance on non-renewable energy sources and decreasing the strain on energy generation and distribution systems.

The adoption of energy-efficient induction motors can also help drive economic growth and job creation. As automobile industries transition to more efficient motor systems, new employment opportunities emerge in manufacturing, research and development.

7

Conclusion and future work

7.1 Conclusion

This thesis presents the detailed analysis of the induction motor in terms of losses, torque ripple and tooth forces when excited with purely sinusoidal voltage feeding and PWM feeding. The machine was modelled with good accuracy as the results from analytical calculations were found to be close to the results from simulation results.

The PWM feeding was successfully implemented with the PWM pulses being generated in MATLAB and imported in the ANSYS Maxwell model as datasets. The computational time to reach steady state was reduced greatly by using purely sinusoidal voltage excitation at the beginning of the simulation and the excitation was switched to PWM once the machine reached the steady state. The results from the FEM simulation in regards to harmonic orders in torque ripple and tooth forces correlate to the theoretical predictions. The dominant force harmonics and torque harmonics are found for orders 0, 2 and $n \pm 1$.

The radial and tangential force acting on the tooth have similar characteristics for both sinusoidal and PWM feeding but with more harmonics with PWM feeding which is expected. The magnitude of the tangential force was found to be consistently decreasing as we move from the tip of the tooth towards the yoke.

The average torque is found to be lower with PWM feeding as compared to the average torque obtained with the sinusoidal feeding. The cause for the lower average value of torque can be attributed increased core loss and copper loss due to increased eddy current loss, hysteresis and increased harmonics in the current waverforms.

When it comes to losses, it is observed that there is a substantial increase in eddy current loss, almost $3-4$ times when the excitation was changed from sinusoidal to PWM. The hysteresis loss saw an increase of around $10-12$ % between the two different excitation while increase in copper loss was just around $3-4$ %. Overall, the efficiency was a bit lower with PWM feeding than with the purely sinusoidal feeding. Nonetheless, with good modulation technique and a proper switching frequency, the efficiency of the motor can be increased further.

7.2 Future work

The effect of inverter, possible cables, etc needs to be included in order to get a more accurate view on torque ripple and losses. The total loss in the system and harmonics could vary with the inclusion of a inverter and cables. The thermal analysis was out of the scope in this thesis, so inclusion of thermal analysis with electromagnetic analysis could help to understand the behavior of the machine accurately as the thermal properties are the major limitation with regards to the operation range. Additional improvements can be made by including the stray losses and extra losses in the induction machine model. Other simulation techniques can be developed to decrease the computational time with PWM feeding and obtain results for more cycles which will provide us with more data to analyze. Further investigation into the why the harmonics content of the perfectly sinusoidal are not present in the PWM could also be a thing of future work. Running a new set of locked rotor and no load test with PWM feeding to get the equivalent circuit parameters during PWM and compare them to the results from perfectly sinusoidal input to see how big the difference may be. It could be of interest to implement the minimum loss controller with an adaptive limiting line taking parameters values who change with frequency and current amplitude into account and not use for example a constant magnetising inductance to make the limiting line more accurate that at the moment.

References

[1] K. H. Chu, M. A. Prabhu, J. Pou, S. Ramakrishna, and A. K. Gupta, "Analysis of Local Forces Acting on Stator Teeth and Magnetic Wedges in Large Synchronous Machines," in *2018 Asian Conference on Energy, Power and Transportation Electrification, ACEPT 2018*, 2019.

[2] W. Zhu, S. Pekarek, B. Fahimi, and B. J. Deken, "Investigation of force generation in a permanent magnet synchronous machine," *IEEE Transactions on Energy Conversion*, vol. 22, no. 3, 2007.

[3] M. R. Raia, S. Ciceo, F. Chauvicourt, and C. Martis, "Influence of Stator Teeth Harmonic Shaping on the Vibration Response of an Electrical Machine," in *EPE 2020 - Proceedings of the 2020 11th International Conference and Exposition on Electrical And Power Engineering*. Institute of Electrical and Electronics Engineers Inc., 10 2020, pp. 193–199.

[4] F. Niu, S. Cao, X. Huang, J. Zhang, K. Li, and Y. Fang, "Analysis of EMI in Motor System Driven by PWM Inverter; Analysis of EMI in Motor System Driven by PWM Inverter," Tech. Rep., 2018.

[5] O. Wallmark, *AC Machine Analysis, Fundamental Theory*. Department of Electric Power and Energy Systems, KTH Royal Institute of Technology, 2018., 2018.

[6] J. Pyrhönen, T. Jokinen, and V. Hrabovcová, *Design of Rotating Electrical Machines*. Wiley, 10 2013.

[7] A. Andersson, "Electric machine control for energy efficient electric drive systems," Tech. Rep.

[8] Lennart Harnesfors, *Control of Variable Speed Drives*, 2002.

[9] Sang-Hoon Kim and S.-K. Sul, "Maximum torque control of an induction machine in the field weakening region," *IEEE Transactions on Industry Applications*, vol. 31, no. 4, pp. 787–794, 7 1995.

[10] Hannah Ritchie, "Cars, planes, trains: where do CO2 emissions from transport come from?" 10 2020.

[11] "CO2 emissions from cars: facts and figures," 2019.

[12] Unfccc, "ADOPTION OF THE PARIS AGREEMENT - Paris Agreement text English," Tech. Rep.

[13] J. Cui, J. Ormerod, D. Parker, R. Ott, A. Palasyuk, S. Mccall, M. P. Paranthaman, M. S. Kesler, M. A. McGuire, I. C. Nlebedim, C. Pan, and T. Lograsso, "Manufacturing Processes for Permanent Magnets: Part I—Sintering and Casting," *JOM*, vol. 74, no. 4, pp. 1279–1295, 4 2022.

A

Appendix 1

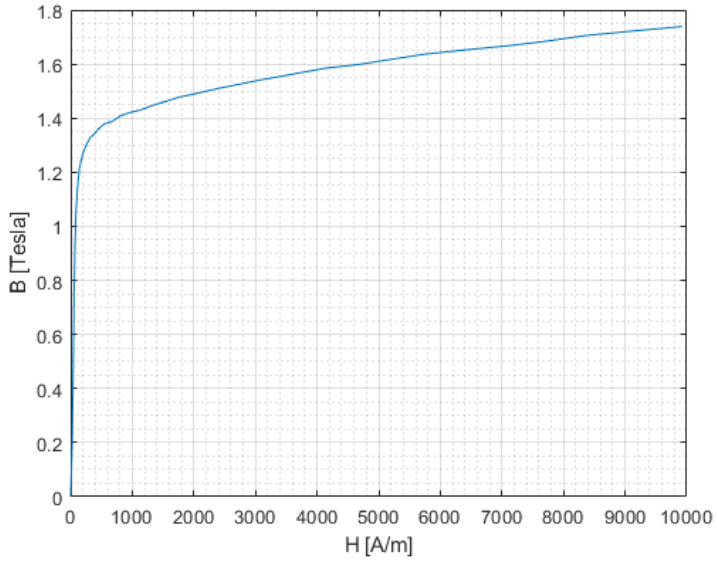

Figure A.1: BH curve for M235-35A

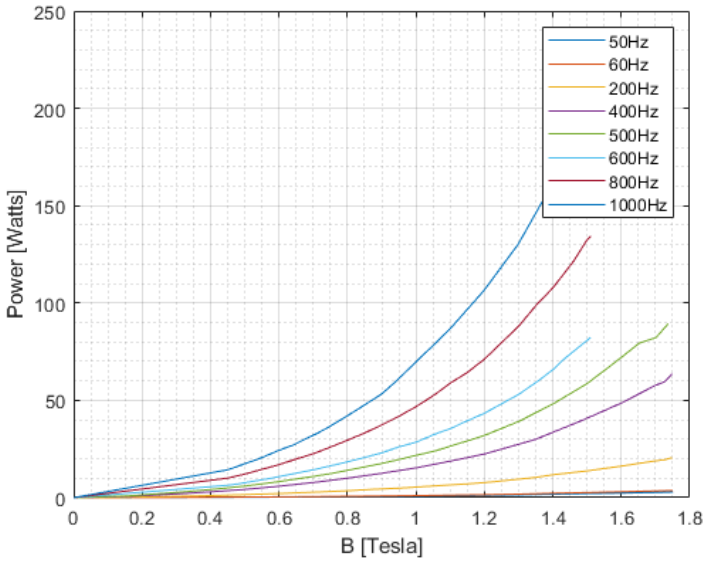

Figure A.2: Frequency vs loss curve for M235-35A

DEPARTMENT OF SOME SUBJECT OR TECHNOLOGY
CHALMERS UNIVERSITY OF TECHNOLOGY
Gothenburg, Sweden
www.chalmers.se

CHALMERS
UNIVERSITY OF TECHNOLOGY